FAIR PAC NuSTAR
FAIR-TAC HISPEC
2014-04-19

Technical Report for the Design, Construction and Commissioning of NEDA@HISPEC

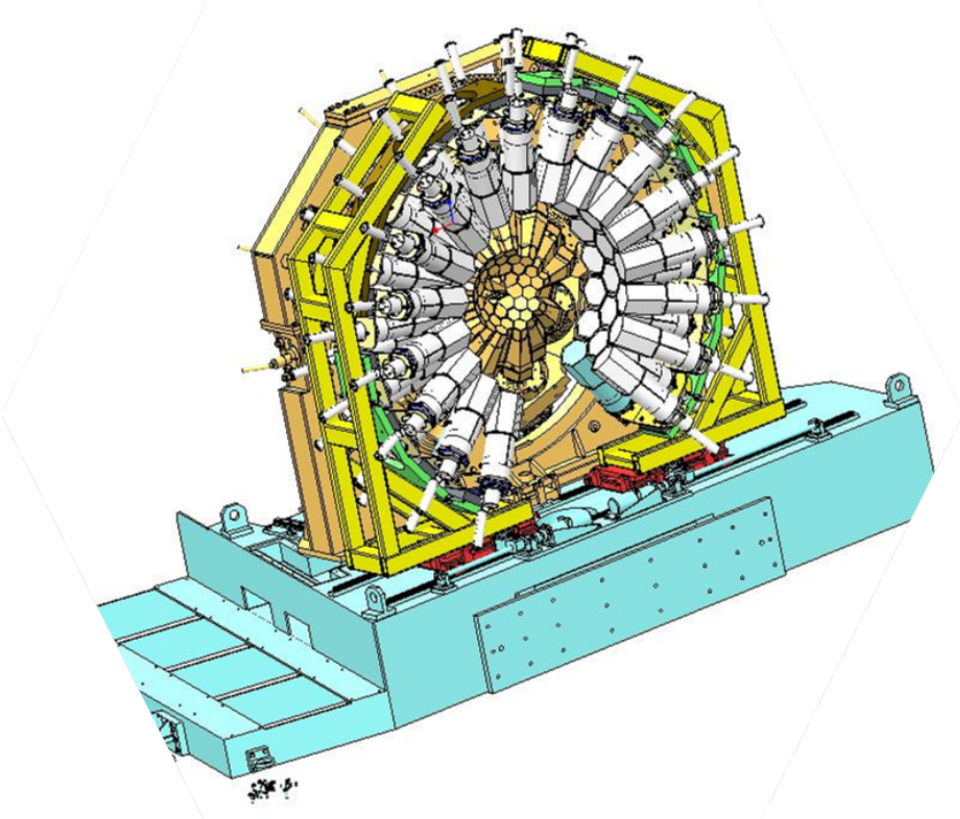

Abstract. The Neutron Detector Array NEDA . . .

Members of the NEDA@HISPEC Collaboration

Uppsala University, Uppsala, Sweden
Johan Nyberg et al.

Royal Institute of Technology, Stockholm, Sweden
Bo Cederwall et al.

Lund University, Lund, Sweden
Dirk Rudolph et al.

University of York, York, United Kingdom
Robert Wadwsorth et al.

IFIC, CSIC-Univ, Valencia, Spain
Andres Gadea et al.

Spokesperson etc. for NEDA@HISPEC

Spokesperson	Johan Nyberg	johan.nyberg@physics.uu.se
Technical Coordinator	N.N.	
Contact Person at the FAIR site	N.N	
Group Leader in Matters of Safety	N.N	

Authors of this Report

Names and affiliation of the full NEDA collaboration ...

Contents

1 Introduction and Overview

This should include information about the full NEDA organisation, a basic description of the standard HISPEC setup (Super FRS, beam tracking detectors before, AGATA around, and LYCCA after the secondary target.

2 Physics with NEDA@HISPEC

In this section a brief description is given of some of the physics cases that will be possible by using NEDA at the HISPEC setup. A more detailed description of an experiment with NEDA@HISPEC to study Gamow-Teller and Isobaric Analog Resonances and neutron-skin effects in neutron-rich nuclei is give in subsection 2.4.

2.1 High-energy beams: 80 - 200 MeV/A

- Inverse kinematics charge-exchange reactions p(X, n)Y for studies of Gamow-Teller and Isobaric Analog Resonances and neutron-skin effects in neutron-rich nuclei. See more details of this in subsection 2.4.
- 1n- and 2n-knockout reactions for studies of proton-rich nuclei. High-energy neutrons emitted in the forward angles. Example: ^{54}Ni→^{52}Ni+2n 87 MeV/A (P.J. Davies et al., PRL 111, 072501, 2013).

2.2 Medium-energy beams: 10 - 100 MeV/A

- Inverse kinematics stripping reactions d(X, n)Y for spectroscopy of proton-rich nuclei, measurement of spectroscopic factors, etc. Low- to intermediate-energy neutrons emitted in the forward hemisphere. Example: d(^{57}Cu, n)^{58}Zn 100 MeV/A (recent experiment with GRETINA at MSU, C. Langer, F. Montes et al.).

2.3 Low-energy beams: 4 - 10 MeV/A

- Fusion-evaporation, and multi-nucleon transfer reactions. "Classical" setup with AGATA in the backward and NEDA in the forward angles. This type of reactions will only be possible in the far future when high-intensity slowed-down beams may become available at NuSTAR/FAIR.

2.4 Isobaric Analog - Spin-Isospin Resonances and the Neutron Distribution in the Sn Isotopes

The availability of radioactive nuclear beams of good intensity and optical quality makes possible the use of charge exchange nuclear reactions to investigate fundamental properties such as the nuclear matter distribution, deformation and the evolution of shell structure very far from stability. The predicted reduction in the spin-orbit term in the nuclear force with increasing neutron excess is believed, together with the tensor component of the residual nucleon nucleon interaction, to be the main origin of the changes in the single particle energies of intruder states and of the shell quenching effects. We propose to investigate using the NEDA detector and the FAIR beams, the energy values of the Gamow-Teller and Isobaric analog resonances for various isotopic chains. Such information is directly linked to the evolution of the spin orbit term for increasing N/Z ratios as well as to the difference in slope between neutron and proton radii.

In recent years experiments with radioactive beams from projectile fragmentation facilities have revealed the presence of a neutron halo in several of the lightest nuclei on the neutron drip line. This structure arise when the last one or two neutrons are in a low angular momentum orbits and close to the top of the potential well so that their wave functions have a very extended distributions which is manifested in an anomalously large matter radius. In heavy nuclei several calculations predict a different phenomenon to occur. An excess of several neutrons build up so that the neutron density extends out significantly further than that of protons, resulting in a mantel of dominantly neutron matter. The presence of such neutron skin is expected to affect collective modes of nuclear excitation which involve the out-of-phase motion of neutrons against protons, such as the Giant Dipole Resonance (GDR) and the scissors mode. There is also the possibility of a soft dipole mode in which the core nucleus move against the more weakly bound skin neutrons. Due to the different slope of the neutron density distribution for larger N/Z ratios, one expects specific terms of the nucleon-nucleon residual interaction, like the spin-orbit term, to be strongly affected or reduced [1, 2, 3, 4, 5].

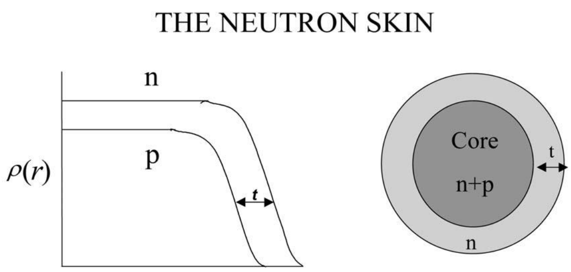

Figure 1: Schematic illustration of the neutron skin. For more extended neutron distributions one expects a reduction of the spin-orbit term of the residual nucleon-nucleon interaction [6].

The predicted reduction in the spin-orbit term in the nuclear force with increasing neutron excess is believed, together with the tensor component of the residual nucleon nucleon interaction, to be the main origin of the changes in the single particle energies of intruder states and of the shell quenching effects.

One of the ways of investigating the difference in slope between the radii of the neutron and proton density distributions along an isotopic chain is based on the measurement of the excitation energies of the Gamow-Teller resonances relative to the isobaric analog states [7]. Nucleons with spin-up and spin-down can oscillate either in phase (spin scalar $S = 0$ mode) or out of phase (spin vector $S = 1$ mode). The spin vector, or spin-flip excitations can be of isoscalar ($S = 1$, $T = 0$) or isovector ($S = 1$, $T = 1$) nature. These collective modes provide direct information on the spin and spin-isospin dependence of the effective nuclear interaction. Especially interesting is the collective spin-isospin oscillation with the excess neutrons coherently changing the direction of their spin and isospin without changing their orbital motion, the Gamow-Teller resonance (GTR) $J^\pi = 1^+$. The simplest charge exchange excitation mode, however, does not require the spin-flip (i.e. $S = 0$) and corresponds to the well known isobaric analog state (IAS) $J^\pi = 0^+$. The spin-isospin characteristics of the GTR and the IAS are related through the Wigner supermultiplet scheme. The Wigner $SU(4)$ symmetry implies the degeneracy of the GTR and IAS, the resonances completely exhausting the corresponding sum rules. The Wigner $SU(4)$ symmetry is however broken by the spin-orbit term of the effective nuclear potential. Therefore the energy difference between the GTR and the IAS is expected to reflect the magnitude of the effective spin-orbit potential. Such dependence and the related effects on the proton and neutron average nuclear radii has been investigated in Ref. [7]. Fig. 2a, extracted from Ref. [7], shows the energy difference between the main component of the

GTR and the respective IAS for the stable $^{112\text{-}124}$Sn isotopes. The experimental data are compared with the results of relativistic quasi-particle random phase approximation model. One notices the systematic reduction of the energy differences when moving towards larger N/Z ratios. Fig. 2b shows the same quantity as a function of the calculated differences between mean neutron and proton radii as well as the systematic dependence of these for increasing mass number in Fig. 2c.

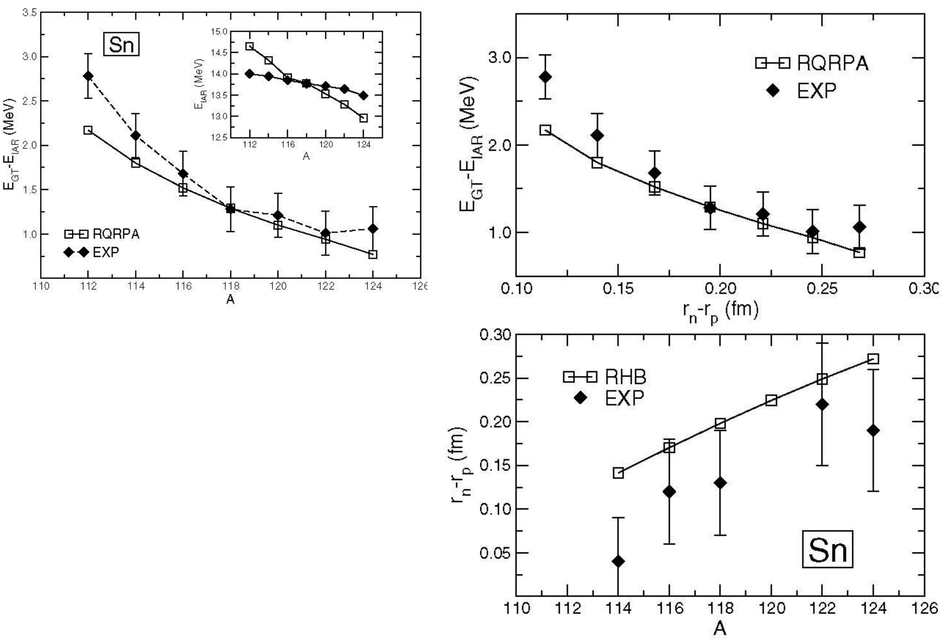

Figure 2: a) The energy difference between the main component of the GTR and the respective IAS for the stable 112-124Sn isotopes extracted from Ref. [7]. The experimental data are compared with the results of relativistic quasi-particle random phase approximation model. In the inset the calculated excitation energies of the isobaric analog states are compared with the experimental results. b) The calculated and experimental energy differences between GTR and IAS as a function of the calculated differences between the rms radii of the neutron and proton density distributions of the even-even Sn isotopes [7]. c) The calculated differences between neutron and proton rms radii compared with the available experimental data.

In this LOI we propose to investigate the energy differences between the GTR and the IAS resonances in different isotopic chains (ex. ^{128,129,130,131,132,133,134}Sn). Such information will allow probing the strength of the spin orbit term of the nucleon-nucleon residual interaction as a function of the N/Z ratio and therefore the mean proton and neutron radii. To populate the GTR and IAS resonances (p,n) reactions have been largely used, Figure 3. We propose to use the charge exchange reaction (p,n) in inverse kinematics [8].

Figure 3 from Ref. [8] shows the triton energy spectra obtained in the ^{118}Sn (^{3}He, t)^{118}Sb reaction at a beam energy of 200 MeV. The beams of ^{128,129,130,131,132,133,134}Sn, produced by the FAIR RIB facility at energies of about 300 MeV/u, will impinge on a H_2 target. The neutrons will be detected at about 90° with energies of a few MeV using the NEDA detectors. From the scattering angle and the TOF measurements the velocity vector and the recoil energy information will be reconstructed with a resolution of about 5 % sufficient to identify the centroid of the GDR. The production rates of the secondary beams ^{128,129,130,131,132,133,134}Sn at the target position are expected to in the order of 10^5 atoms/s to 10^8 atoms/s.

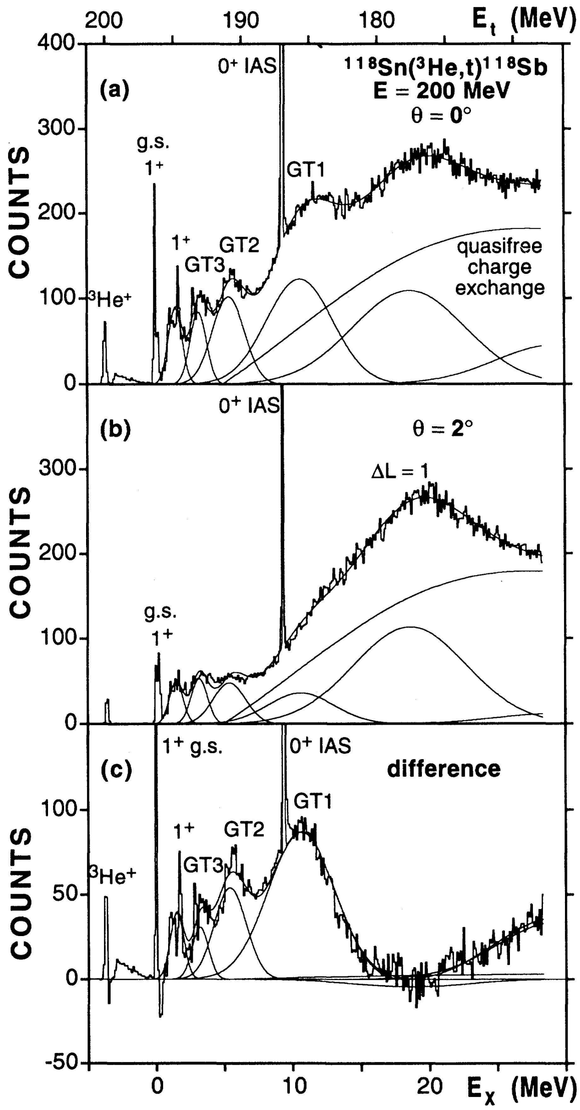

Figure 3: Triton energy spectra from Ref. [8] for the ^{118}Sn(^{3}He, t)^{118}Sb reaction at a beam energy of 200 MeV and (a) $\theta = 0^\circ$ and (b) $\theta = 2^\circ$. (c) shows the difference between (a) and (b). The IAS and GTR resonances are clearly visible. For more details see Ref. [8].

3 Summary of Prototype Results

4 Summary of Physics Simulations

5 NEDA Detector Unit: Simulations

5.1 GEANT4 and principles of neutron detection

The GEANT4 package was the selected tool for the simulations of the NEDA array, due to its flexibility and the possibilities to include a large number of different materials and detector shapes. Moreover, the NEDA array will be used together with γ-ray detector arrays, like AGATA [9], EXOGAM [10], GALILEO [11] and PARIS [12], and with charged particle detectors like DIAMANT [13], EUCLIDES [14], and CUP [15]. GEANT4 models of most of these devices exist, and as consistent simulations of the complete detector setups are often necessary, the use of GEANT4 for the NEDA simulations was imperative. The simulations which are presented here were performed in the framework of the AGATA simulation code [16], which greatly facilities combining all the above mentioned devices in one simulation.

Significant deficiencies of the neutron interaction model NeutronHP included in GEANT4 versions earlier than 4.9.2 are, however, known. The results presented in this paper were obtained with GEANT4 versions 4.9.2.p02 and 4.9.3 in which an attempt to correct the neutron interactions was made [17]. We decided anyway that the applicability of the model to our purpose should be verified. Firstly, we have compared GEANT4 generated angular distributions of neutrons elastically scattered on protons, deuterons and carbon nuclei to cross-sections of the ENDF VII data base [18], and the agreement was found to be good. Secondly, we have also checked the processes activated in GEANT4 when neutrons interact in the scintillator liquid and analysed the spectra of the energy deposited in the scintillator by neutrons. This analysis is presented below. Note that earlier versions of the GEANT4 NeutronHP model were not correctly reproducing the angular distributions. The list of possible processes and the energy spectra were also incorrect. Finally, two existing neutron detectors were irradiated with radioactive sources, and their measured performance was compared to the simulations, see Section 5.2.

Simulated histograms of the energy deposited by 10 MeV neutrons in a cylindrical scintillator volume are shown in Fig. 4. The processes responsible for the different structures in the histograms are indicated in the plots. In a hydrogen-based scintillator, the most important interaction of neutrons with an energy of a few MeV is elastic scattering on protons. This reaction gives rise to an isotropic distribution of the recoiling protons [19, 20] in the centre-of-mass system, see also Ref. [21]. This leads to a flat proton energy distribution extending from zero to the energy of the incident neutron. A neutron, however, in a large volume detector usually undergoes a series of such interactions which sometimes leads to a deposit of the full energy of the neutron in the detector. This is the reason for the peak at 10 MeV in the spectra shown in Fig. 4.

At lower energies, the spectrum exhibits pronounced irregularities, which are due to interactions with ^{12}C. The sharp edge at 4.299 MeV is due to the endothermic reaction ^{12}C(n, α)^{9}Be ($Q =$ –5.701 MeV). The two produced charged particles deposit their entire kinetic energy close to the interaction point. Another sharp edge is seen at 5.561 MeV in the spectra in Fig. 4. It is due to the deposit in the detector of the full energy of neutrons that have undergone inelastic scattering on ^{12}C, populating the first excited state at 4.439 MeV in ^{12}C that decays by the emission of a γ-ray, which escapes from the detector. The trapezoidal shape between 7.26 MeV and 7.86 MeV indicates an incorrect functioning of GEANT4. The events leading to this shape originate from the reaction ^{12}C(n, α)^{9}Be, which never should lead to an energy deposit larger than 4.299 MeV. We have also noted that the reaction ^{12}C(n, n')3α is missing in the list of GEANT4 processes. The cross section for this reaction is, however, not significant for neutron energies up to 10 MeV. The low-energy part of the spectrum, below 2.5 MeV, is dominated by elastic scattering on ^{12}C. Counts visible in Fig. 4a above the incident neutron energy of 10 MeV are due to exothermic capture on protons.

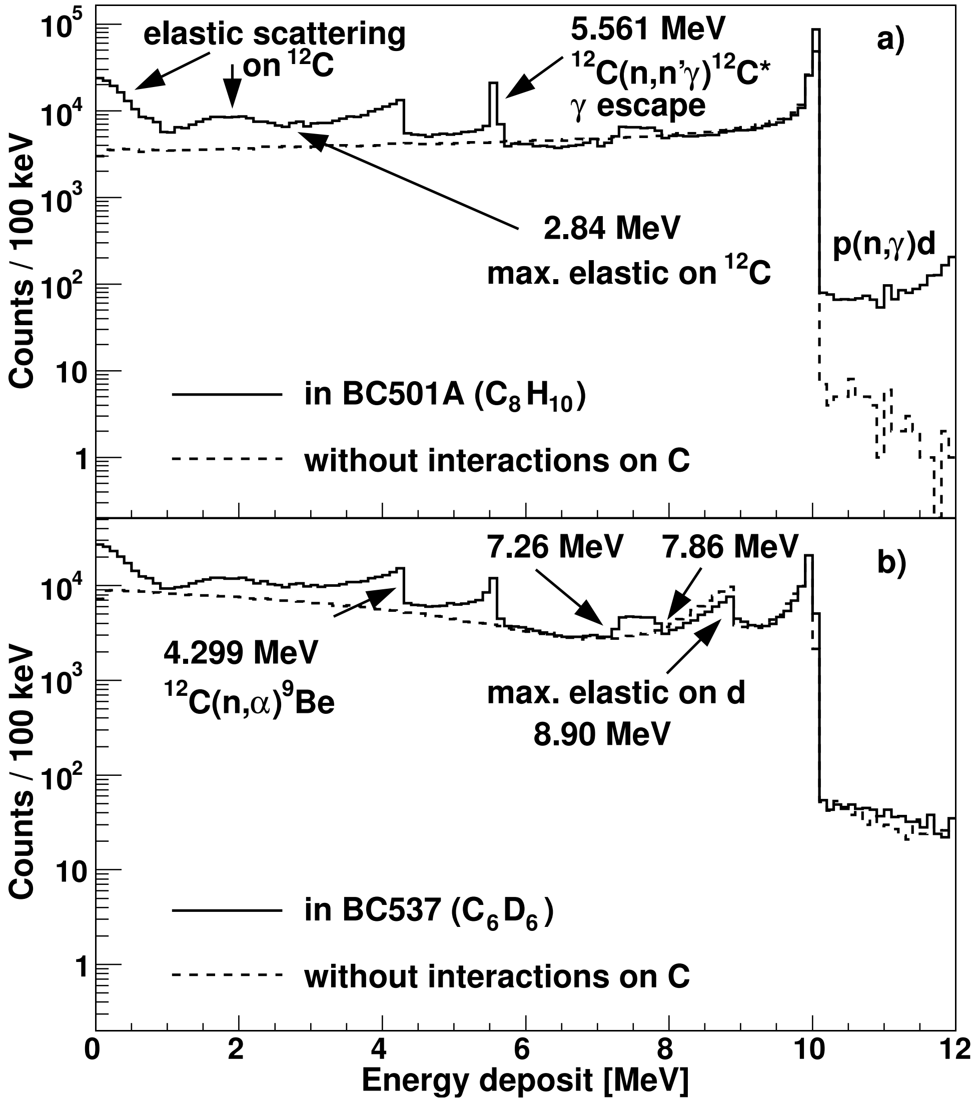

Figure 4: Geant4 simulation of the energy deposited by 10 MeV neutrons in the two liquid scintillators (a) BC501A (C_8H_{10}) and (b) BC537 (C_6H_6). The detectors have a diameter of 12.7 cm (5 inch) and a length of 20 cm. The detector walls were not included in the simulations. The energy-deposit spectra for the hypothetical detector material consisting only of protons and deuterons (without carbon) are drawn with dashed lines.

The spectrum of the energy deposit in the deuterated scintillator (Fig. 4b) resembles the one obtained for the proton based material, with the additional edge at 8.9 MeV which corresponds to the maximal single interaction energy transfer to a deuteron. Also, the spectrum slopes up at low energies, which reflects the anisotropy (forward and backward angles favoured) in scattering of neutrons on deuterons. Note that in the deuterated scintillator the relative number of events with full energy deposit is smaller than in the case of the proton based scintillator. In about 9% of events neutrons in the deuterated scintillator cause endothermic breakup of ^{2}H ($Q = -2.552$ MeV), and in 55 % of these events energy is not properly conserved in Geant4. The Q values calculated from kinetic energies of products of such reactions are distributed between –5 MeV and more then 10 MeV. Events of this kind, with the positive, erroneous Q-values, are responsible for counts visible above 10 MeV in Fig. 4b.

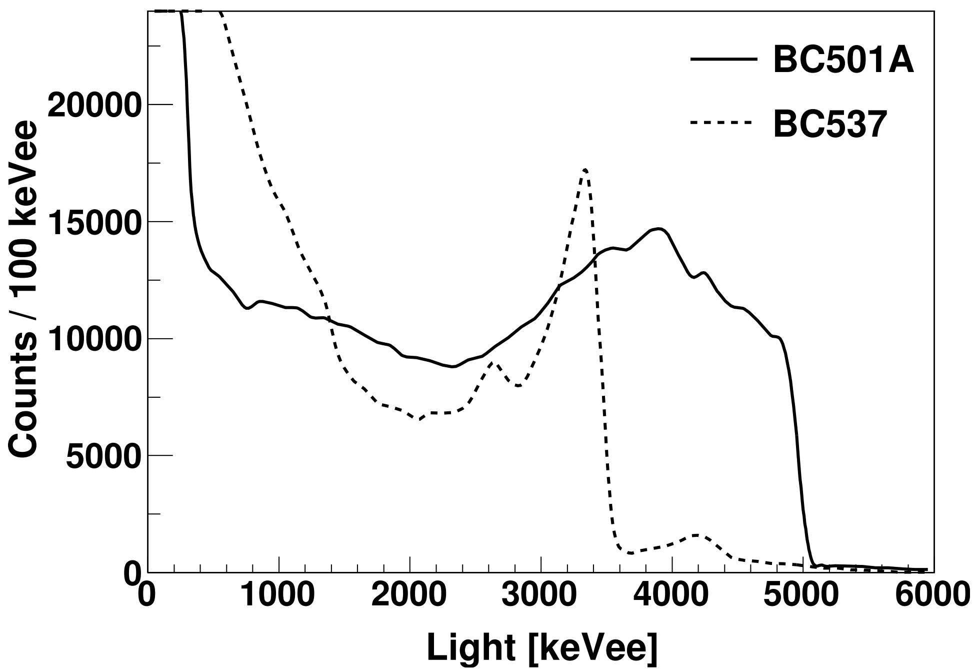

Figure 5: GEANT4 simulation: scintillator light output for 10 MeV neutrons in the detector of Fig. 4. An instrumental response function was not included in this calculation.

The neutron induced reaction products, or secondary particles produced in subsequent interactions, deposit energy in the scintillator and this energy is converted in our simulations to scintillation photons (light) using the parametrisation of reference [22]. Light may be produced by protons, deuterons, α particles, ^{9}Be and ^{12}C nuclei as well as by electrons and γ rays. The amount of light produced strongly depends on the type of particle moving in the scintillator. It is largest for electrons and γ rays and it is reduced for heavier particles. The unit 1 keVee (keV electron equivalent) is used for the light output (yield). It is the amount of light produced when an electron deposits an energy of 1 keV in the scintillator.

The light output for the scintillator cylinders used for Fig. 4 is shown in Fig. 5. The drastic difference between the shapes of the histograms of the produced light and of the deposited energy indicates the difficulties of obtaining direct information on the energy of the neutrons. Unlike the spectra of the deposited energy, the light histograms peak at zero energy. The majority of the events with very low light output are due to interactions on ^{12}C. Note that in a real measurement, the spectra are affected by the instrumental response function, which smears out the structures visible in Fig. 5, see Sections 5.2 and 5.6.

Experimentally, detectors count (register) neutrons (or γ rays) if the amplitude of the signal from the detector photomultiplier exceeds a certain level. The time of the detection is determined using for example a constant fraction discriminator. A similar procedure was applied in the simulation taking into account that each neutron usually interacts many times in the detector volume. In order to reproduce the experimental situation as close as possible, we first time sort the interactions, then sum them up incrementally. The "detection" time of the signal produced is defined as the time when the light produced in the detector exceeds the assumed threshold. In the following discussion, we use the term *significant interaction*, which refers to a series of interactions leading to a signal above threshold. A threshold of 50 keVee is assumed for most of the calculations presented in this work, except in section 3 in which a larger threshold was used for a part of the data.

The analysis outlined above leads to the conclusion that the elastic scattering process on protons, deuterons and on ^{12}C is well reproduced in Geant4. Deficiencies of inelastic scattering on ^{12}C and ^{2}H were still identified. These deficiencies do not affect the results of the present work, as they contribute only to a small fraction of the neutron interaction cross section in the interesting neutron energy range. In addition the amount of light produced in reactions on ^{12}C is much lower than in scattering on protons or deuterons.

5.2 Experimental validation of the simulation

In order to further validate the GEANT4 simulations, experimental data were collected with two existing neutron detectors and the results were compared with the simulations. One of the detectors was a NORDBALL neutron detector [23] which is made of a hexagonally shaped steel vessel, see Fig. 6, containing 3.9 litre scintillation liquid of the type BC501 [24]. The other detector had a cylindrical shape with a diameter of 153 mm, length of 135 mm and contains 1.8 litres of the same scintillator.

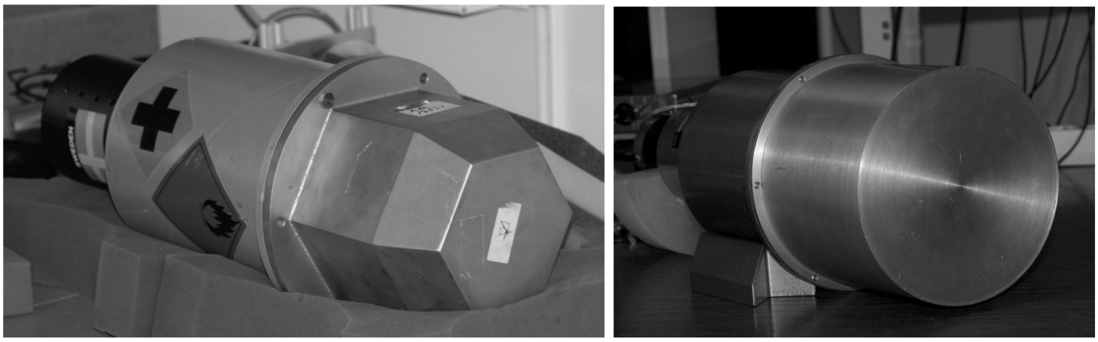

Figure 6: Neutron detectors used in the test measurements: NORDBALL detector (left) and the cylindrical detector (right).

The detectors were irradiated by γ rays from the radioactive sources ^{137}Cs, ^{22}Na and ^{207}Bi, as well as by γ rays and neutrons from ^{252}Cf sources. GEANT4 models were created for the two detectors and the simulations were run for both neutrons and γ rays. The content of the ^{250}Cf isotope in the neutron sources was taken into account in the data evaluation and simulations. The source used in the measurements with the NORDBALL detector was 35 years old, and at the time of the measurement it was emitting $6.0 \cdot 10^3$ and $4.3 \cdot 10^3$ neutrons per second, in the fission of ^{250}Cf and ^{252}Cf, respectively (compare Ref. [25]). The source used with the cylindrical detector was isotopically more pure, with 110 and $3.9 \cdot 10^3$ neutrons per second respectively emitted by the two isotopes. In the simulations it was assumed that the neutron energy distributions of both Cf isotopes were identical, and were given by the expression from Ref. [26]: $N(E) = \sqrt{E}\exp(-E/T)$, where $T = 1.42$ MeV.

The measurements with the NORDBALL detector were performed at Uppsala University. The liquid was viewed through a glass window by a 14-stage, 5 inch diameter photomultiplier tube (PMT) of the type Philips XP2041. The high voltage used was –1.75 kV. The anode signal of the neutron detector was sent to an NDE-202 NIM electronic module [27]. This unit has a built-in circuit for neutron-γ discrimination based on the zero cross-over (ZCO) technique. It produces a TAC output signal corresponding to the time difference between the leading edge of the input signal, which is obtained from an internal constant fraction discriminator (CFD), and the ZCO time. The neutron-γ discrimination is done by setting a limit on the ZCO TAC amplitude. The NDE-202 unit also has a built-in charge-to-voltage-converter (QVC), which produces a signal proportional to the collected PMT charge. The ZCO TAC and the QVC signals were sent to a multichannel analyser system containing a 8192 channel peak-sensing ADC. The number of detected neutrons, which is needed for the determination of the neutron detection efficiency (see below), was obtained by integrating the number of counts in the neutron peak in the ZCO spectrum shown in Fig. 7a.

The measurements with the cylindrical 1.8 litre detector took place at the Heavy Ion Laboratory in Warsaw. The PMT was of type XP4512B and the voltage used was –1.6 kV. The anode signal was digitised by a CAEN DT5720 12 bit, 250 MS/s digitiser connected to a laptop computer via a USB 2.0 cable. The readout of the data was triggered at time t_0, when the signal exceeded a threshold of an internal leading edge discriminator (LED) of the digitiser. The number of collected sampling points for each waveform was 64, including 17 samples acquired before t_0. The digitiser had to be protected against too large input signals. A LeCroy 428F fan-in–fan-out unit, which limits the amplitude to a maximum of –1.77 V, was therefore placed between the detector and the digitiser. The dead-time of the digitiser was estimated by using a signal from an ORTEC 448 Research Pulser that was fed into one channel of the digitiser. Neutron-γ discrimination was performed off-line by using the charge comparison method [28, 29], see Fig. 7b. The two charge values needed for the discrimination, Q_{fast} and Q_{slow}, were obtained by integrating signals in the time intervals (t_0, $t_{max} + 20$ ns) and ($t_{max} + 20$ ns, $t_{max} + 60$ ns), respectively, where t_{max} is the time when the maximum of the signal height was detected. Neutron energy spectra were produced by integrating the area of the digitised waveforms.

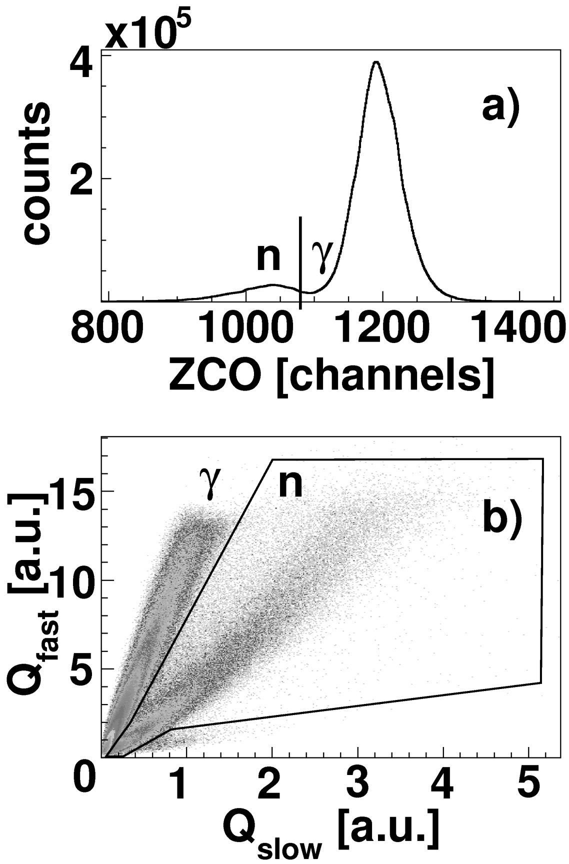

Figure 7: Zero-cross-over time (ZCO) histogram (a) and two dimensional charge comparison plot (b) used for the neutron-γ discrimination in the Uppsala and Warsaw measurements, respectively. See text for the definition of Q_{fast} and Q_{slow}.

The data collected with γ-ray sources enabled calibration of the output signals in units of keVee. Background spectra were also measured and were subtracted from the spectra acquired with the sources, taking into account data taking times and the estimated dead times of the setups.

The resulting γ-ray spectra obtained with the NORDBALL detector are shown in Fig. 8a-c. The broad peaks seen in the spectra are Compton edges of the respective γ rays. Simulations indicate that the actual Compton edge energy value corresponds to about 90% of the peak height to the right

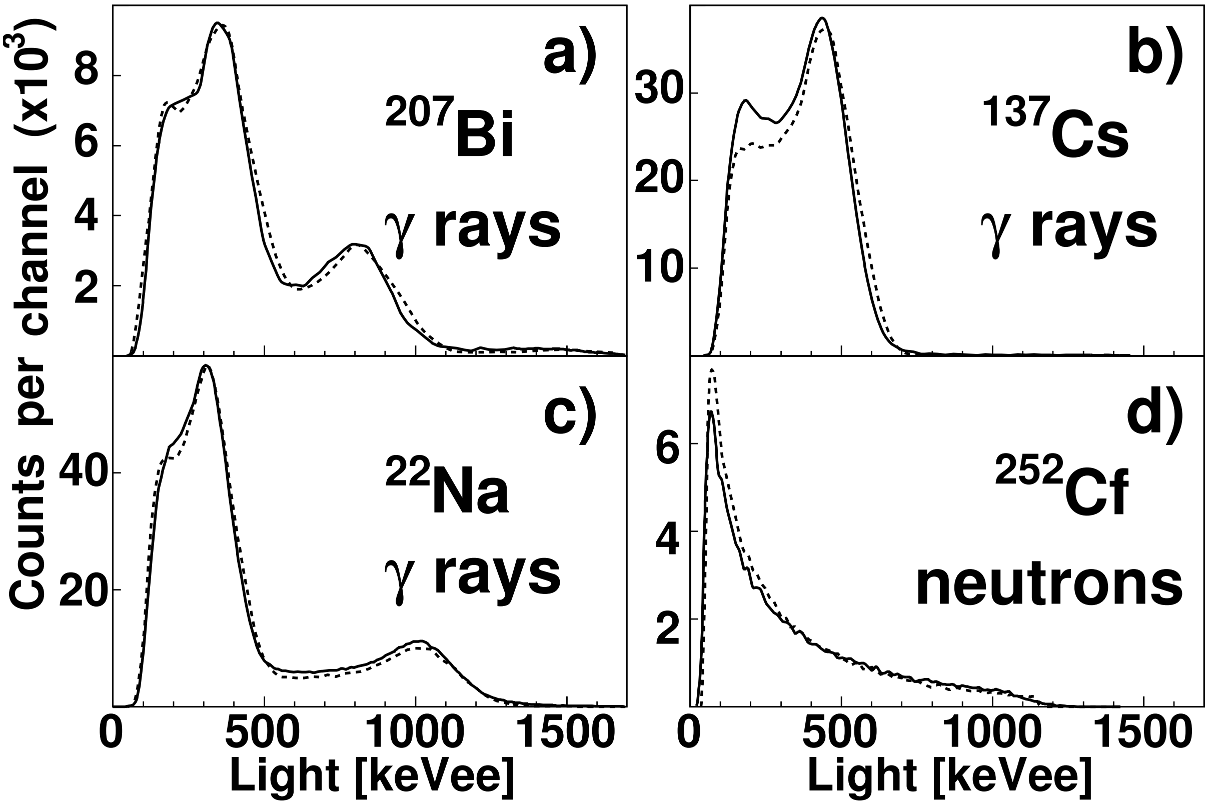

Figure 8: Experimental (solid) and simulated (dotted line) γ-ray spectra for the NORDBALL detector (a-c) and a neutron spectrum for the cylindrical detector (d). The simulated γ-ray spectra shown in plots (a) and (c) are normalised to the maximum of the experimental distributions, while the ^{137}Cs γ-ray and ^{252}Cf neutron histograms show true measured and simulated numbers of counts, corresponding to the source activity. The ^{207}Bi and ^{22}Na sources were placed at a distance of 20 cm from the front of the detector, while for ^{137}Cs and ^{252}Cf this distance was 50 and 5 cm, respectively.

of the maximum of the peak. Based on such γ-ray calibration points, the threshold (CFD or LED) values could be converted to keVee units, resulting in 115 keVee and 50 keVee for the Uppsala and Warsaw measurements, respectively. With known calibration and threshold values, the simulated spectra can be compared with the measured ones for both γ rays and neutrons, see Fig. 8. The light yield values (L) obtained in the simulation were randomised using a Gaussian distribution to account for the statistical effects of the light production, attenuation, photon to electron conversion and electron amplification. The standard deviation (σ) of this distribution was assumed to be proportional to $\sqrt{L}$ and the proportionality factor was adjusted to reproduce the width of the bump at Compton edge in the experimental ^{137}Cs spectrum, resulting in $\sigma = 1.9\sqrt{L}$. The same Gaussian smearing function was used for the calculations presented in the following sections.

The exact activities of the ^{207}Bi and ^{22}Na sources were not known, and thus the simulated spectra in plots a) and c) of Fig. 8 are normalised to the maximum of the experimental distributions. On the other hand, the ^{137}Cs and ^{252}Cf histograms show absolute numbers of counts obtained in the experiment and in the simulation for the same numbers of emitted γ rays and neutrons, taking into account the activities of the sources.

The shape of the simulated γ-ray spectra agrees well with the measurements. The most notable difference is in the energy range 100-400 keVee in the ^{137}Cs histogram for which a larger number of counts were measured than what was obtained in the simulations. This effect could be attributed to γ rays scattered from the surrounding material into the detector, an effect that was not included in the simulations. We note however, that it is not clear why a similar discrepancy is not seen in ^{22}Na and ^{207}Bi γ-ray spectra in Fig. 8. Nevertheless, the absolute ^{137}Cs γ-ray efficiency is rather

	Efficiency (%)			
	absolute		intrinsic	
Detector and radioactive source	exp.	sim.	exp.	sim.
NORDBALL:				
^{137}Cs γ rays, 50 cm	0.30(1)	0.285(1)	0.50(2)	0.476(7)
^{252}Cf neutrons, 51 cm	0.174(9)	0.241(2)	0.30(2)	0.419(4)
Cylindrical:				
^{252}Cf neutrons, 5 cm	6.1(3)	6.64(2)	0.283(14)	0.306(1)

Table 1: Comparison of the measured and simulated efficiency of the two neutron detectors. The intrinsic efficiency values were calculated as a ratio of the absolute numbers and the fraction of the solid angle covered by the front faces of the detectors. Distances between the sources and the front faces of the detectors are given in the first column. See the text for the discussion of the presented uncertainties.

well reproduced and is presented in Table 1.

In the low light part of the neutron spectrum the simulations give more counts than the measurement. One possible reason for this difference is that the neutron-γ discrimination works less well for signals with a small light yield, which leads to a loss of neutrons in the measurements [29]. Another explanation may be a problem of the threshold determination, for example due to a possible non-linearity of the energy calibration at low light yields. Note that the lowest γ-ray calibration point was at 341 keV (Compton edge of the 511 keV γ-ray). The threshold value was obtained by an extrapolation of the energy calibration to lower energies. The threshold position significantly influences the neutron detection efficiency as the neutron light distributions strongly peak at zero. It is also seen in Fig. 8 that all the simulated spectra are shifted to slightly higher energies compared to the measured spectra. This effect could be corrected for by changing the linear calibration coefficient by about 4%. The total neutron detection efficiency of the two detectors was calculated and compared with the simulations, see Table 1.

The experimental uncertainties given in Table 1 include statistical errors, errors of the data taking time determination (including dead time effects) and uncertainty of the source activities at the time of the measurement (which is the dominating uncertainty of the three mentioned here). The uncertainty of the neutron-γ discrimination for the ^{252}Cf sources is not taken into account. In case of the discrimination using the analogue ZCO value (the NORDBALL detector) this uncertainty is difficult to estimate, and likely leads to loosing a significant fraction of neutrons. This may explain the observed difference between the efficiency values obtained in the measurement and simulation for the ^{252}Cf neutrons in the NORDBALL detector. The agreement obtained for neutrons detected in the cylindrical detector is better. We anyway also in this case expect significant uncertainty of the neutron-γ discrimination, leading to an about 15% error bar on the number of the detected neutrons. Note that the imperfect neutron-γ discrimination may also lead to erroneous increase of the measured neutron detection efficiency, if some γ rays are misinterpreted as neutrons. We conclude that a satisfactory agreement between the measurement and simulation was obtained.

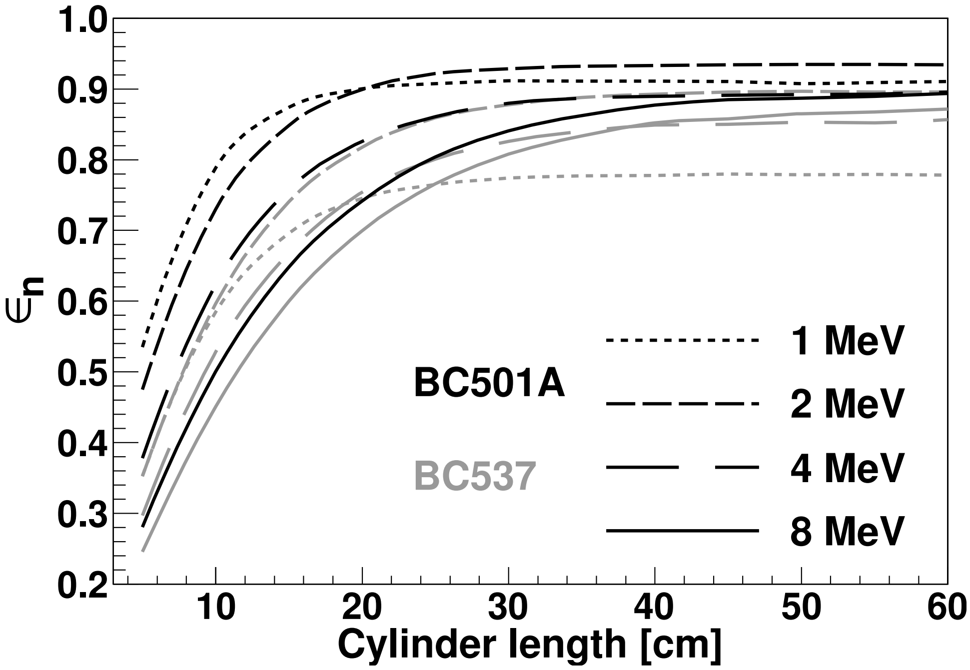

Figure 9: Neutron detection efficiency (ϵ_n) as a function of the cylinder length for the two scintillators BC501A (black lines) and BC537 (grey lines) and for 1, 2, 4 and 8 MeV neutrons.

5.3 Optimum depth of the detector

In the attempt to find an optimum size of the NEDA detector modules, a systematic study was performed to determine the depth of the scintillator detector that is needed in order to register a significant interaction.

A pencil beam of monochromatic neutrons was shot into a scintillator cylinder with a 50 cm diameter and variable length. No detector walls were included in this simulation and the neutron detection efficiency was analysed as a function of the length of the cylinder. The efficiency to detect a neutron, was defined as $\epsilon_n = N_{detected}/N_{emitted}$, where $N_{emitted}$ and $N_{detected}$ are the number of neutrons which were emitted and which created a significant interaction, respectively. The diameter was deliberately chosen to be rather large (50 cm), so that the detection probability depended only on the cylinder length and was not influenced by a limitation of the diameter. The results of this study are presented in Figure 9.

The neutron detection probability as a function of the cylinder length reaches a constant value of about 80 to 95%, at a cylinder length of 20 to about 40 cm depending on the neutron energy and the type of the scintillator. A further increase of the detector length does not lead to a significant increase of the detection probability. Reaching an efficiency of 100% is not possible, because in some events neutrons lose energy in reactions which do not produce enough light to exceed the threshold.

We also analysed the depth distributions of the significant interactions. The results shown in Fig. 10 corroborate the above observations based on Fig. 9. The majority of the interactions take place within the first layers of the scintillator (depending on the neutron energy), but the tails of the depth distributions are large, thus the thickness of the scintillator necessary to detect almost all neutrons is also large (compare Fig. 9). The lowering of the mean significant interaction depth at 4 MeV (see insert of Fig. 10) is attributed to the fact that elastic scattering on carbon becomes significant only at this energy (carbon nuclei moving in the scintillator are able to produce enough light). Thus, the total interaction cross section increases at about 4 MeV. In turn, at 5.561 MeV the $^{12}C(n,\alpha)^{9}Be$ reaction channel opens, but the products of this reaction need another 2–3 MeV of kinetic energy to be detected, and therefore the significant interaction depths become smaller only at about 8 MeV.

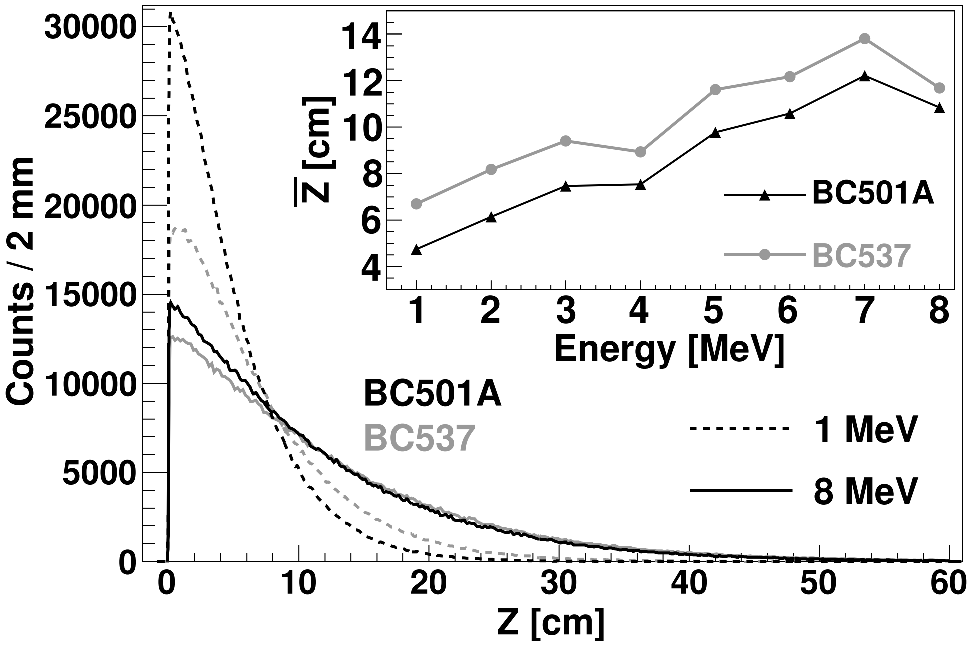

Figure 10: Distributions of the depth of the significant interaction (Z) for two neutron energies and two scintillators, BC501A and BC537. The type of the scintillator is marked with black and grey lines for BC501A and BC537, respectively. The line pattern marks the neutron energy as shown in the legend. A total of 10^6 neutrons were simulated in each case. The insert shows the dependence of the mean significant interaction depth ($\overline{Z}$) on the neutron energy. Lines connecting the points in the insert are drawn only to guide an eye.

We conclude that for most of the neutrons emitted in fusion-evaporation reactions, the maximum of the detection efficiency will be reached at a detector length of 20 to 30 cm. Increasing the detector length by another 10 or 20 cm would lead to slightly larger efficiency for the fastest neutrons. Two additional factors should, however, also be taken into account in determining the optimum length of the detector. The first one is the influence of the detector length on the probability that one neutron generates a signal in more than one detector. This is discussed further in section 5.4. The second factor is the relation of the detector size to the quality of the neutron-γ discrimination. This effect was not studied in the present work, but the results presented in Ref. [30] indicate that the discrimination deteriorates for larger detectors.

5.4 Transverse size (diameter) of the detector

Neutrons undergo significant interactions mainly along the axis of their incoming direction. Distributions of the significant interaction with respect to this axis are shown in Fig. 11. After the first interaction, a scattered neutron may however produce another significant interaction, which is located far away from the initial axis, usually in another detector module. In order to study the distribution of such second significant interactions a setup was evaluated consisting of two coaxial detectors, an inner and an outer detector as shown in Fig. 12. Such a setup is a good representation of a detector module surrounded by a number of other modules, with unimportant geometrical details omitted.

A pencil beam of monochromatic neutrons was directed to the centre of the inner detector. The probability to register a significant interaction in the outer detector was evaluated for events in which the central detector fired, with the inner cylinder diameter varied within the range from 5 to 30 cm. The outer diameter of the setup was 1 m and detectors with two different lengths were used: 20 and 40 cm. The results are shown in Fig. 13. The plotted values are defined as $P_{1n\to 2n} = N_2/N_1$, where

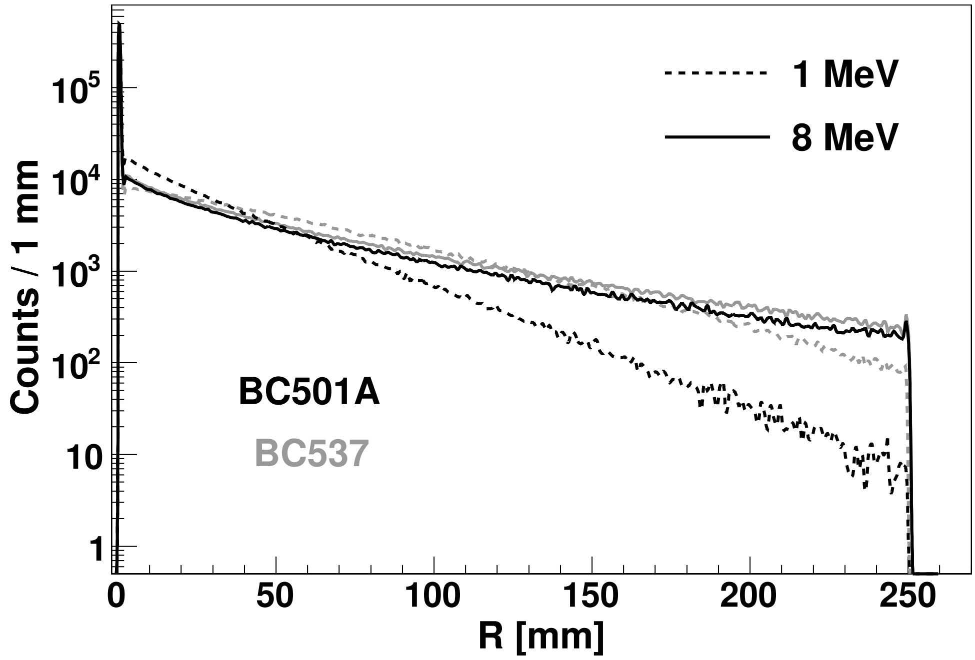

Figure 11: Distribution of the distance (R) between the position of the first significant interaction and the axis of the incoming neutrons. The results of the simulations for two neutron energies (1 and 8 MeV) are shown with black and grey lines for the two scintillators, BC501A and BC537, respectively. A pencil beam of 10^6 neutrons were shot into the centre of the cylindrical detector in each of the presented cases.

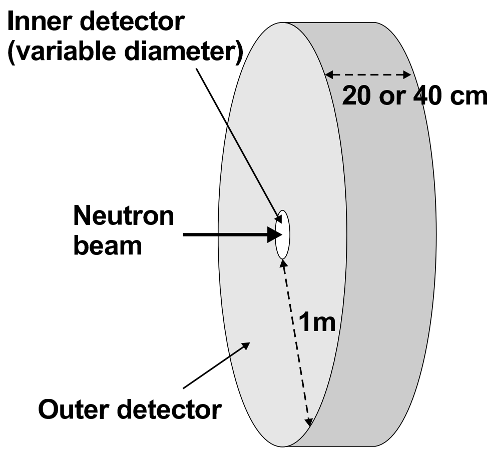

Figure 12: Setup used in the evaluation of the probability that one neutron generates a signal in more than one detector module.

N_1 and N_2 are the number of neutrons which gave significant interactions in the inner cylinder and in both cylinders, respectively.

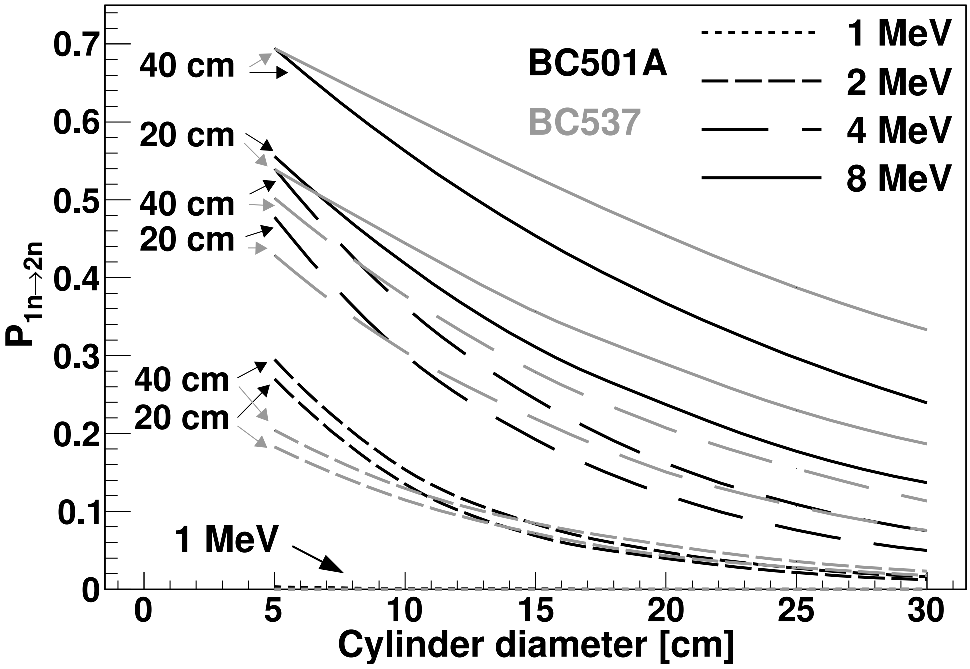

Figure 13: The probability to have an interaction in two detector modules ($P_{1n\to 2n}$) as a function of the cylinder diameter. Four sets of lines, corresponding to neutron energies 1, 2, 4 and 8 MeV, are shown for each of the two scintillators, BC501A and BC537 in black and grey, respectively. Cylinders with two lengths, 20 and 40 cm, were used and the respective lines are marked with text labels and arrows.

Figure 13 indicates that $P_{1n\to 2n}$ is reduced rather slowly with the inner detector diameter. For any practical detector diameters the $P_{1n\to 2n}$ values will be large and if $P_{1n\to 2n}$ values below 1% are required (compare Ref. [31]) additional cleaning conditions of the interactions in two detectors cannot be avoided.

The $P_{1n\to 2n}$ values are significantly larger for longer detectors, for all energies and for both scintillators. The BC501A scintillator gives larger $P_{1n\to 2n}$ values than BC537 for the smallest diameters, but this relation inverts with the increase of the diameter, depending also on the energy of neutrons.

5.5 Times

A larger detector may in principle have worse time resolution. This may also impose an important limitation on the detector size, as the time-of-flight parameter is used to distinguish neutrons and γ rays detected in the scintillator as well as for the 1n/2n discrimination. Two different components contribute to the time resolution of a neutron detector:

- intrinsic time resolution, related to the time required to produce and collect the light signal in the scintillator, and to the electronic jitter;
- varying time-of-flight due to a distribution of significant interaction depths in a thick detector

The intrinsic time resolution cannot be evaluated in our simulations, as light production processes and light transportation are not included in the model. It was, however, experimentally shown in Ref. [32] that the intrinsic resolution of BC501A detectors does not significantly vary with the cylindrical detector length. A value of about 1.5 ns was obtained.

The time-of-flight resolution of a cylindrical detector (the same one as described in Section 5.3) was evaluated as a function of the cylinder length. The widths of the time-of-flight distributions are presented in Fig. 14. Here, the intrinsic time resolution of the detector was not taken into account, and the presented values reflect only the variations of the interaction depths.

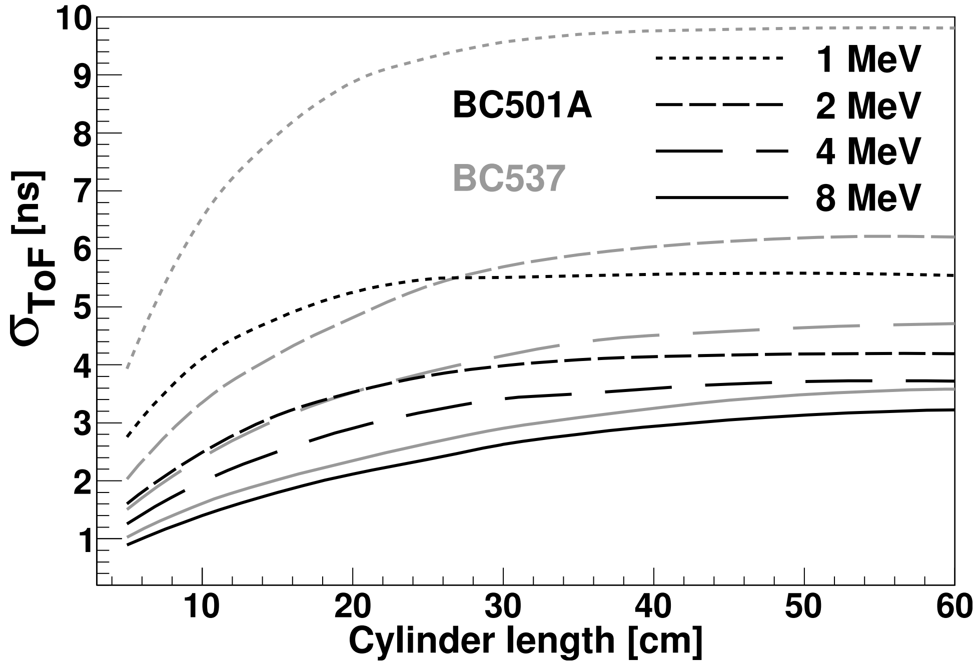

Figure 14: Width (one standard deviation) of the time-of-flight distributions as a function of the cylinder length for BC501A (black lines) and BC537 (grey lines), and for 1, 2, 4 and 8 MeV neutrons.

The width of the time-of-flight distributions as a function of detector length initially rises rather steeply, while for longer cylinders (above 30 cm) it saturates at a certain value. Thus, our simulations do not indicate any limit on the detector length imposed by the time-of-flight resolution. Larger neutron energies lead to smaller time-of-flight variations, which is due to the fact that for a faster particle, variations in the significant interaction depth are less important in terms of time-of-flight. Filling the detector with the BC537 scintillator liquid, results in a significantly worse time-of-flight resolution than in the case of BC501A.

Timing effects are important for the $P_{1n\to 2n}$ probability. Neutrons interacting in the scintillator usually undergo a series of elastic interactions with the nuclei of the medium and then thermalize or escape from the detector. Thus, light is mostly produced within a few nanoseconds after the neutron enters the detector. Scattering of thermilized neutrons in the scintillator may, however, continue for much longer times (up to milliseconds). If a thermilized neutron is captured by a proton, this leads to a very late light flash, due to the registration of the γ-ray emitted in this process. Such effects are more significant for the BC501A scintillator than for BC537, because the cross section for the p(n,γ)d interaction is much larger than for d(n,γ)t. This is illustrated in Fig. 15, which shows times of the interaction in the outer detector of the setup shown in Fig. 12. Indeed, for BC501A, a significant interaction in the outer detector either happens within the first 100 ns, or much later, with an almost flat distribution up to hundreds of μs. The corresponding spectrum for the BC537 scintillator shows no such late light-flash effect.

The late light flash is often produced far from the initial neutron interaction point, i.e. usually in another detector module. Thus, the BC501A scintillator seemingly shows much larger $P_{1n\to 2n}$ values than BC537, if light collection is not limited in time. This is illustrated in Fig. 16 in which $P_{1n\to 2n}$ values of the two scintillators are compared for calculations with and without a 100 ns time limit for the significant interaction. This indicates the importance of properly setting time limits

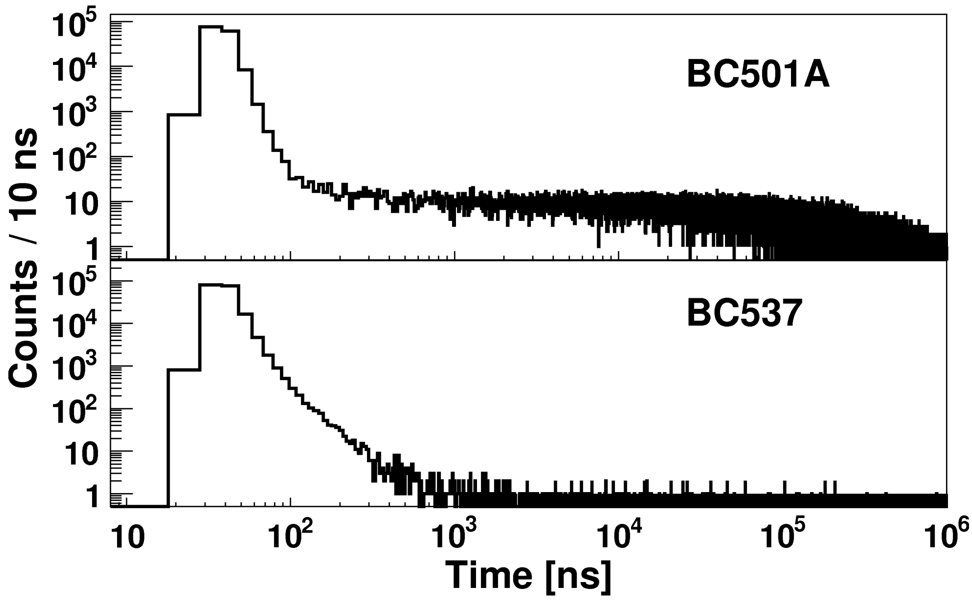

Figure 15: Times of the significant interaction in the outer detector of the two scintillators shown in Fig. 12. A source of 2 MeV neutrons was placed 51 cm in front of the detectors and the time measurement starts when a neutron is emitted from the source. The detectors were 20 cm long and the diameter of the inner detector was 12.7 cm.

on the collection of neutron signals, both in experiments and in simulations. For the efficiency and $P_{1n\rightarrow 2n}$ evaluations presented in this paper, a time limit of 100 ns from the emission of neutrons or γ rays to the first significant interaction was used. Light produced in each detector volume was integrated during 300 ns after the significant interaction.

5.6 Comparison of the two scintillators

As mentioned before, the elsewhere reported advantage of the deuterated scintillator (BC537) is its ability to give a better detector response, i.e. signals which are more proportional to the energy of the incoming neutron, than scintillators based on ^{1}H (like BC501A). Figure 17 shows simulated light spectra produced by a pencil beam of 2 MeV neutrons interacting in two cylindrical detectors filled with BC501A and BC537, of two different sizes: a small detector with a 5 cm diameter, a 5 cm length and a volume of 0.1 litre and a large one with a diameter of 12.7 cm, a length of 20 cm and a volume of 2.5 litre. The large detector has a size that likely will be similar to the size of the NEDA detector module. It can be seen in Fig. 17a that the small BC537 detector indeed gives a pronounced bump corresponding to the incident neutron energy. This bump is not seen in the histogram of the small BC501A detector. However, in the big detector (Fig. 17b), events in which most of the neutron energy is transferred to the scintillator medium in one interaction are relatively rare, and no advantage related to the angular distributions of a single neutron scattering can be observed. Instead, events with multiple neutron interactions dominate, leading to very similar shapes of the spectra for both scintillators. The main difference is that less light is produced in BC537 than in BC501A.

It has already been shown (Fig. 9), that the BC537 scintillator has a lower efficiency than BC501A. The difference between the two scintillators is additionally illustrated in Fig. 18 in which the detection probability for the cylindrical detector is plotted as a function of neutron energy. Note that at low neutron energies, below 1 MeV, the efficiency difference between the two scintillators is very significant.

It should be pointed out that the observed difference between the two scintillators comes mainly from

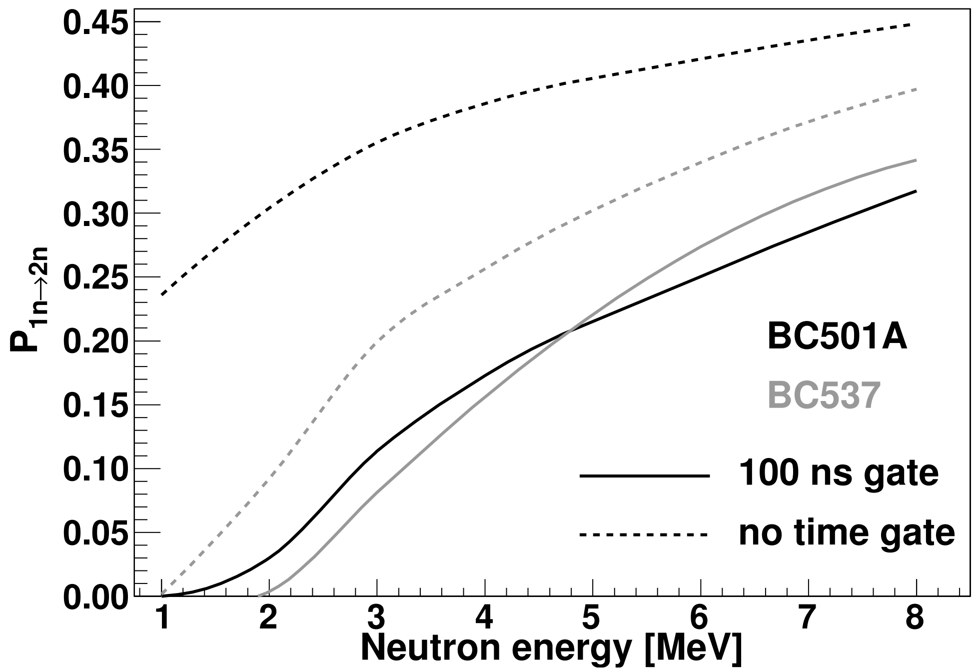

Figure 16: Influence of the 100 ns detection time limit on the $P_{1n \to 2n}$ probability.

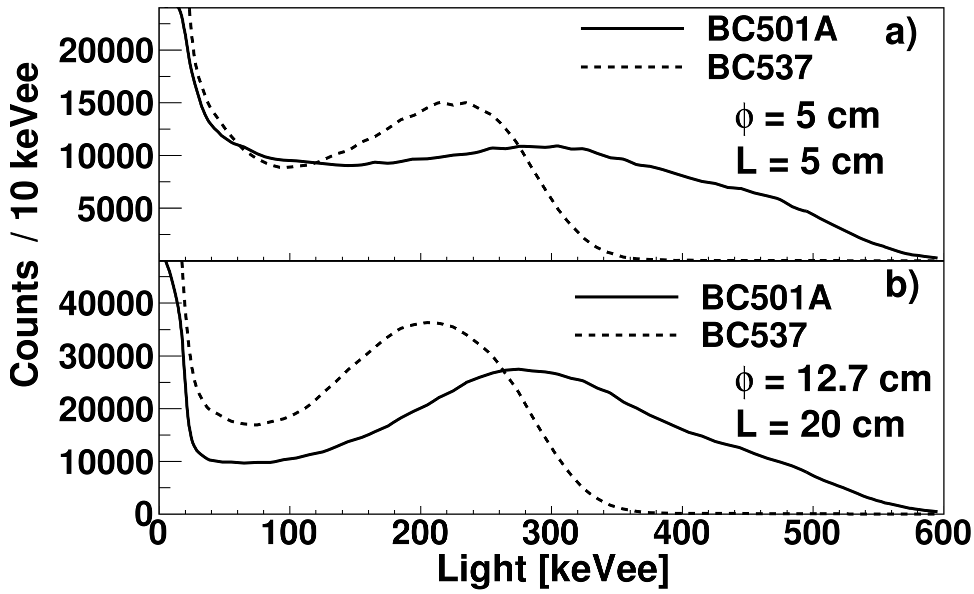

Figure 17: Light produced by a pencil beam of 2 MeV neutrons in two cylindrical BC501A and BC537 detectors of different size: a) a small and b) a large detector. The dimensions of the detectors are shown in the legends.

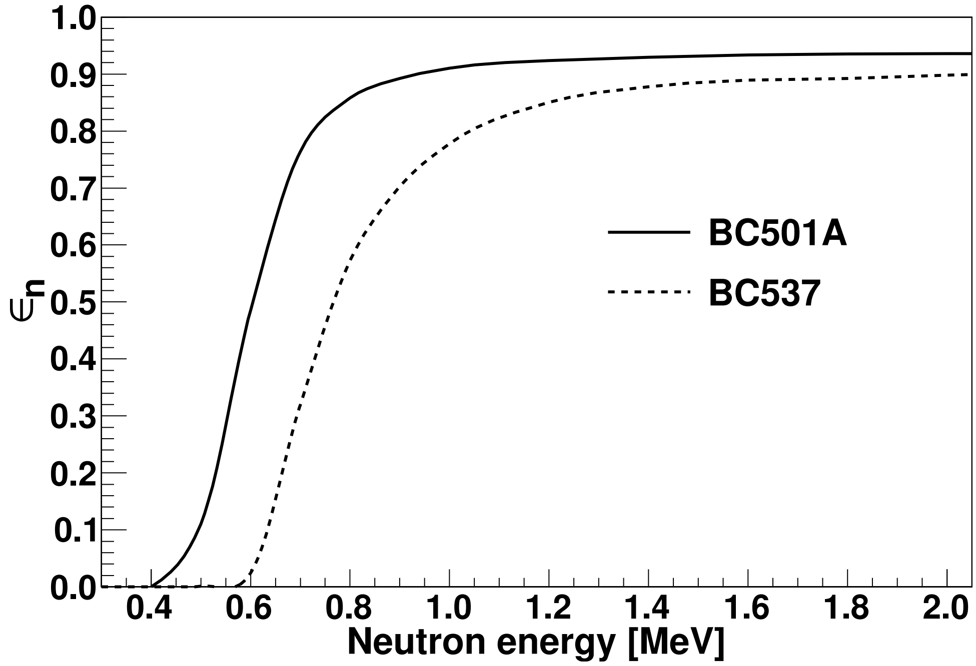

Figure 18: Neutron detection efficiency as a function of neutron energy for the two scintillators BC501A and BC537. The detector had a diameter of 50 cm and was 60 cm long.

the higher cross section for the neutron interaction with protons than with deuterons. In addition, there is relatively more carbon in BC537 (C_6D_6) than in BC501A (C_8H_{10}) and interactions on carbon give very little light. Also, less light is produced per MeV by deuterons than by protons. Thus, the results of the simulations are easily explained by the physical properties of the scintillation material. A smaller amount of light also results in broader time of flight distributions. As far as the $P_{1n \to 2n}$ probability is concerned, both detectors exhibit similar behaviour, except for the situations when the efficiency of BC537 is too low to register two significant interactions. We conclude that based on the simulations we see no advantage of using the deuterated scintillator instead of the standard one.

6 NEDA Detector Unit: Mechanical Design and First Prototypes

V. Modamio et al.

7 Conceptual Design and Simulations

7.1 Conceptual Design

Regular polygons are possible to tile on a surface, and it is possible to make tiling without leaving any gap using only one polygonal shape or a combination of polygonal shapes. A regular hexagon is the only polygon that has the maximum number of edges which can be tiled without leaving gaps and without necessity to use of a combination of more than one polygonal shapes. Therefore a hexagonal prism has been selected as the starting point of the geometry. It has been simulated with a side length of 76 mm (Fig. 19). It was discussed the optimum depth of the cells as 20 cm by G. Jaworski et al.[33]. This was done, as well, to mimic the cell sizes of the Neutron Wall detectors to compare two arrays. An aluminum encapsulation with 2 mm thickness is also added to the detector geometry.

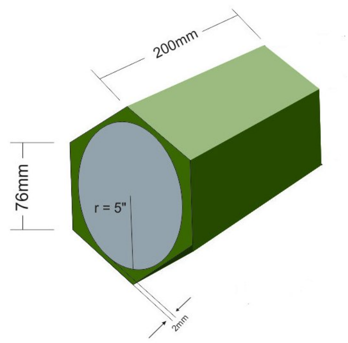

Figure 19: A view from the unitary cell for building up the NEDA array.

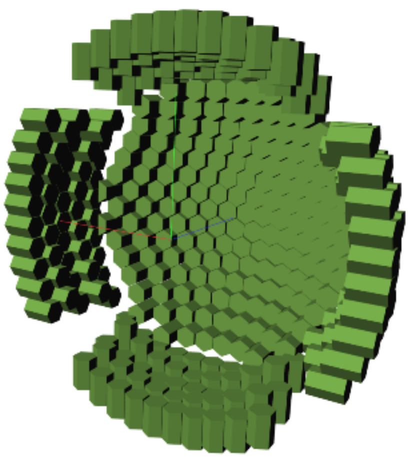

Figure 20: The staircase-like configuration of NEDA. Geometrical efficiency is maximized by traslating the cells in the opposite direction of the beam downstream. The cells between $\theta = 60^{\circ}$ and $\theta = 90^{\circ}$ have been rotated for the maximum exposition to the emitted particles.

In order to have a detector array which is easy to adapt to many laboratories in Europe, NEDA is thought to have a modular design. With a modular geometry, the detector array can be adapted to different experimental conditions. With such motivation, the unitary cells shown in Fig. 19 are tiled to form the new array, and a flat wall-like array has been created as the first configuration of the NEDA geometry. In order to maximize the geometrical efficiency with the optimum number of detectors, the cells which are positioned between $\theta = 0^{o}$ and $\theta = 60^{o}$ have been traslated in the opposite direction of the beam downstream to form a spherical surface. Then the cells which are between $\theta = 60^{o}$ and $\theta = 90^{o}$ have been rotated 90^{o} in their ϕ axis to maximize the exposition to the emitted particles. Such geometry covers around 1.88 sr solid angle and is shown in Fig. 20.

Additionally to the configurations built with the unitary detector cells, the configurations with spherical surface have also been created. In these configurations, 16 different irregular hexagonal shapes has been used to form the array. Considering the diffuculties in production process, costs, and the covered solid angle with the given volume (see Table 2), these configruations were created within the academic research purposes.

An early implementation of NEDA build coupling the NEDA detectors with the Neutron Wall array has been proposed for the AGATA campaign at GANIL planned to be done in the year 2015. The new detector array (i.e. NEDA + the Neutron Wall) will cover almost 2π solid angle, and thus will have high geometric efficiency. More information regarding the geometry is provided on Table 2.

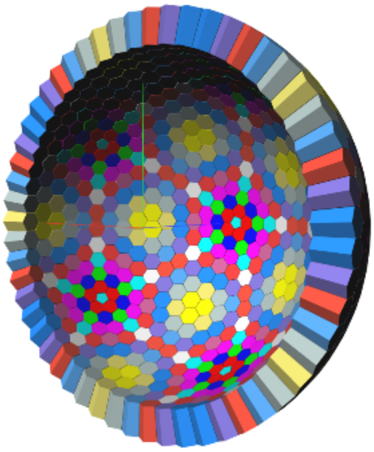

Figure 21: The spherical configuration has been designed basicaly for the academic study. They are not feasable to produce in terms of machinery and budget.

Geometry	Solid angle coverage	Cell volume	Total Volume	Granularity	Radius
Staircase 2π	1.88 sr	3 l	1065 l	355	1.0 m
Spherical 2π	2 sr	2 l	1212 l	606	1.0 m
Neutron Wall	1 sr	3 l	145 l	50	0.5 m
NWall + NEDA	1.90 sr	3 l	313 l	102	0.5 m

Table 2: Physical properties of different configurations

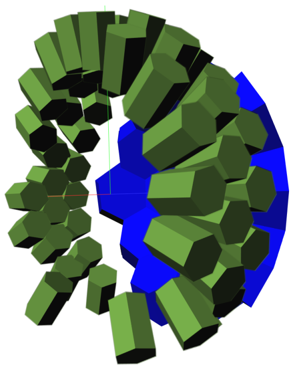

Figure 22: The proposed geometry for the possible NEDA and the Neutron Wall coupling for the AGATA campaign at GANIL, planned in the year 2015.

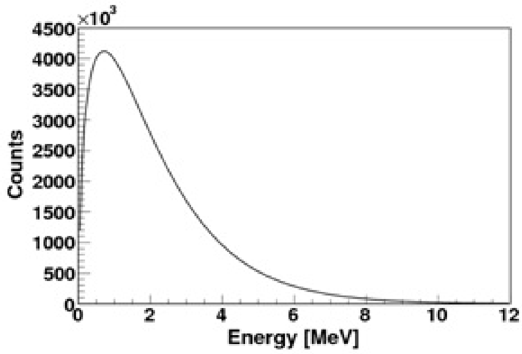

Figure 23: Neutron energy distribution of a ^{252}Cf source versus intensity according to eq. **??**

7.2 The Event Generator

The simulations have been performed both the internal event generator of GEANT4 [34, 35] and *PACE*4_*Na*97 code [36]. Neutrons with an energy distribution sampled from a ^{252}Cf source were produced using the internal event generator of GEANT4. The intensity as a function of energy has been taken from ref [37] and follows the equation:

$$N(E) = E^{1/2}e^{-E/T} \tag{1}$$

The energy distribution with respect to intensity which is suggested by eqation **??** is shown on Fig. 23.

Neutrons from an evaporation reaction have been calculated with the *PACE*4_*Na*97 code. The chosen reaction is ^{58}Ni (220Mev) on ^{56}Fe (thick target). The motivation to chose this reaction is due to existence of a comprehensive work previously done [31], and thus to have a good reference point to evaluate the simulations in this study. The most populated 2p1n and 2p2n channels have been taken concerning to have enough statistics.

New optical model parameters (OMPs), which are used to calculate transmission coefficients (Tl) have been implemented in the *PACE*4_*Na*97 code. The calculations have been carried out using the largely adopted parametrisation described by Hodgson [6] and a more recent one proposed by Koning and Delaroche [4]. The authors have fitted the OMPs with the available systematics of elastic scattering of neutrons and protons with nuclei in the following mass and energy ranges:

- Hodgson: $24 < A < 132$ and $E = 1 - 30MeV$ (where the imaginary spin-orbit term is null);
- Koning: $24 < A < 209$ and $E = 0.2 - 200MeV$.

Koning and Delaroche constructed asymmetry-dependent neutron and proton global OMPs which not only improve the description of the observables with respect to all the other existing phenomenological OMPs, but also cover wider mass and energy ranges. These OMPs have been successfully adopted in a recent systematic work [7] to reproduce the cross section measured in the neutron and proton induced reactions and they have the properties required for calculations involving nuclei far from stability.

In Fig. 24 neutron and proton energy spectra in the laboratory system are shown for the complete angular range for calculations using the two OMPs. In both cases and mostly for the protons, the spectra are softer when the Koning OMPs are used, while at low energies the two OMPs give very similar results. The large differences in the proton transmission coefficients at low energy strongly

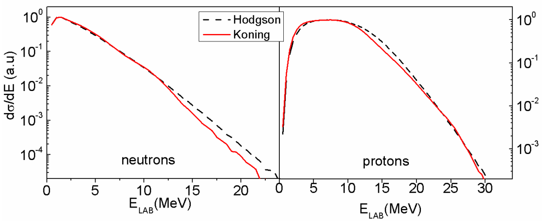

Figure 24: Total neutron and proton energy spectra from the decay of the compound nucleus ^{114}Xe at $E^* = 54 MeV$, obtained by $PACE2\_Na97$ by using the two different OMPs.

Decay Channels	σ_{1n} (μb)	σ_{2n} (μb)	σ_{3n} (μb)	$\sigma_{2p1\alpha}$ (μb)	$\sigma_{1p1\alpha}$ (μb)
Hodgson	9.9	131	1.7	109	39
Koning	5.7	97	2.4	63	74
Difference	-42%	-25%	41%	-42%	89%

Table 3: Fusion-evaporation cross sections of Xn and the two strongest channels for the reaction ^{58}N at 220 MeV on ^{56}Fe. Row 4 shows the difference in percent between row 2 and 3.

modify the neutron-proton competition, as can be seen in Table 3. The channels where more than 1 neutron released are the most interesting ones for future nuclear structure experiments to be performed with NEDA. Results for these channels are shown in the table together with the strongest reaction channels. While the effect on the energy spectra, by using the two different OMPs, is small, the difference in the particle emission probabilities produces a significant modification of the cross sections for both weak and strong reaction channels. The observed differences cannot be estimated *a priori*, in fact they originate from the interplay of the model ingredients when describing the emission probabilities. The fusion-evaporation code follows the de-excitation of the compound nucleus on event-by-event basis recording the history of each decay step. The energy spectra and spatial distribution of the emitted light particles in the laboratory system can be extracted by ltering the results with the geometry of the detectors, providing a reliable comparison to the experimental data [38]. The angular and energy distributions of 2n and 3n channels are shown in Fig. 25. Obviously, the mean energy of the neutrons emitted in the 2n channel is higher than in the 3n channel, which implies that the neutrons of the 3n channel are more focused in the forward direction, clearly it can be seen when comparing the yield ratios at small and large angles. The knowledge of the spatial distribution of the emitted neutrons is essential in order to be able to define the angular coverage of the detector array and its efficiency for a given reaction.

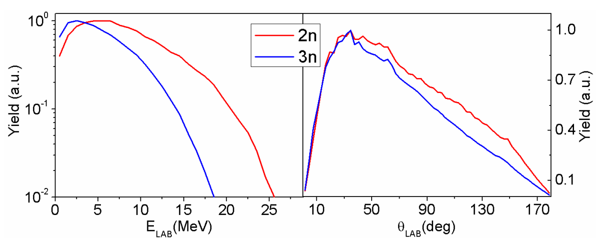

Figure 25: Angular distribution and energy spectra of neutrons emitted in the 2n and 3n reaction channels following the decay of the compound nucleus ^{114}Xe at $E^* = 54 MeV$.

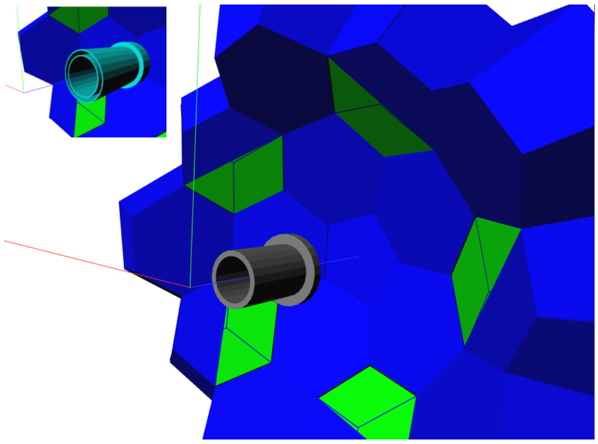

Figure 26: The setup of the Neutron Wall (blue) and the beam line and beam dump after the target (gray, stainless steel) as modeled in GEANT4. The small picture on the upper left corner shows the intersection of the stainless steel pipes (turquoise).

7.3 The Neutron Wall Simulations

The threshold energy of the detectors is one of the crucial parameters in neutron detection. In fact it affects all the observables that characterize the performances of detection setup: efficiency, angular distribution and ToF spectra. The energy threshold used in our simulations were determined using the calibration runs performed with ^{207}Bi γ-ray source collected just before the ^{58}Ni+^{56}Fe experiment. The thresholds energies could be determined for all Neutron Wall detectors and they were included individually in the simulations. The average value of the thresholds of the 43 detectors of the Neutron Wall was determined as around 150 keVee. Seven detectors were inoperative during the experiment, and correspondingly these detector counts were removed from the simulations, nevertheless, the scattering events due to these detectors have been taken into account.

The geometrical design of the Neutron Wall array allows us to group the detectors according to their polar angles with respect to the beam direction. There are 7 groups of detectors which have similar angles in the Neutron Wall.

Besides the Neutron Wall geometry, some of the material between the target and the Neutron Wall was also included in the simulations: two concentric beam lines with a thickness of 2 mm and a CF100 vacuum flange, which was used as a beam dump. See Fig. 26.

7.4 Results and Discussion

Results of the simulations for each configuration are shown on Table 4 and Table 5, for neutrons sampled from a ^{252}Cf source and from the fusion evaporation reaction, respectively.

As it is seen clearly from the results, the flat geometries have a disadvantage in terms of the efficiency, on the other hand they are quite flexible. Taking into account this concern, the Staircase-like geometries are both better considering the efficiency performances and the fact that one can always modify the focal point and thus the array can be fit any experimental environment. The sphere-based geometries are the best when the efficiency matters. As they consist of the detector cells with 16 different irregular hexagonal shape, the production process would be more complicated and expensive.

Geometry	Material	ϵ_{1n}	ϵ_{2n}	ϵ_{3n}
Staircase 2π	BC501A	18.83%	3.83%	1.07%
Staircase 2π	BC537	12.30%	1.56%	0.30%
Spherical 2π	BC501A	22.61%	3.57%	0.81%
Spherical 2π	BC537	15.27%	1.65%	0.28%
Neutron Wall	BC501A	10.66%	0.64%	0.07%
NW + NEDA	BC501A	18.32%	2.54%	0.69%

Table 4: Simulation results of the ^{252}Cf source for different configurations

Geometry	Material	ϵ_{1n}	ϵ_{2n}	ϵ_{3n}
Staircase 2π	BC501A	47.35%	X%	X%
Spherical 2π	BC501A	55.33%	X%	X%
Neutron Wall	BC501A	32.94%	X%	X%
NW + NEDA	BC501A	41.25%	X%	X%

Table 5: Simulation results of the fusion evaporation reaction for different configurations

8 Front-End Electronics

8.1 Electronics Layout

NEDA electronics design is going to be separated in three phases. Firstly, the new digital electronics are envisaged to instrument for the former Neutron Wall detector, containing of 45 detectors. In parallel, during the development of NEDA, 45 more scintillator detector modules are expected to be coupled in 2015. The coupling with AGATA and other detectors has to be foressen. The electronic chain is built of the following parts: the front-end single-ended to differential converters, the sampling Mezzanines and the NUMEXO2 pre-processing, the LINCO2 PCIe interfqace, the Global Trigger and Synchronization (GTS) and the workstations for data acquisition and processing. Each single detector module is readout by one single Front-End Electronics channel whenever a current signal is provided from the corresponding a PMT. Those current signals are connected to the front-end connection panel, coping with the conversion to differential before sending the signal through a 10m cable to the NUMEXO2 digitizer. Each conversion board contains a total amount of 8 channels to convert. Once the signal reaches the digitizer NUMEXO2, the pulse is sampled periodically by the FADC Mezzanines [39] at 200 Msps with a resolution of 14-bits. The FADC Mezzanines are part of the NUMEXO2 digitizer being each board plugged onto the motherboard. As the signal is digitized, it passes by a set of programmable devices based on FPGA: a Virtex-6 and a Virtex-5. Firstly, a trigger algorithm is applied in the Virtex-6 so that the amount of events produced by gamma-rays get drastically reduced, optimizing hence the readout bandwidth capabilities. At the Virtex-5 trigger requests, produced mostly by neutrons, are received and sent to the GTS (Global Trigger System) in order to receive a validation or rejection. A timestamp is as well attached to the event buffer. Additionally inside the Virtex-5, an embedded processor containing an embedded Linux OS runs the slow-control tasks of the whole digitizer and the communication ports. Each NUMEXO2 digitizer has the capability to deal with 16 channels and contains one optical connection to the GTS. In Fig. 27, the global electronics layout is depicted for a total amount of 45 detectors, requiring 3 NUMEXO2 NIM boards. The local GTS in the NUMEXO2 card is connected optically to the GTS tree installed in another NIM modules, although the connection procedure and number is detailed in the GTS section.

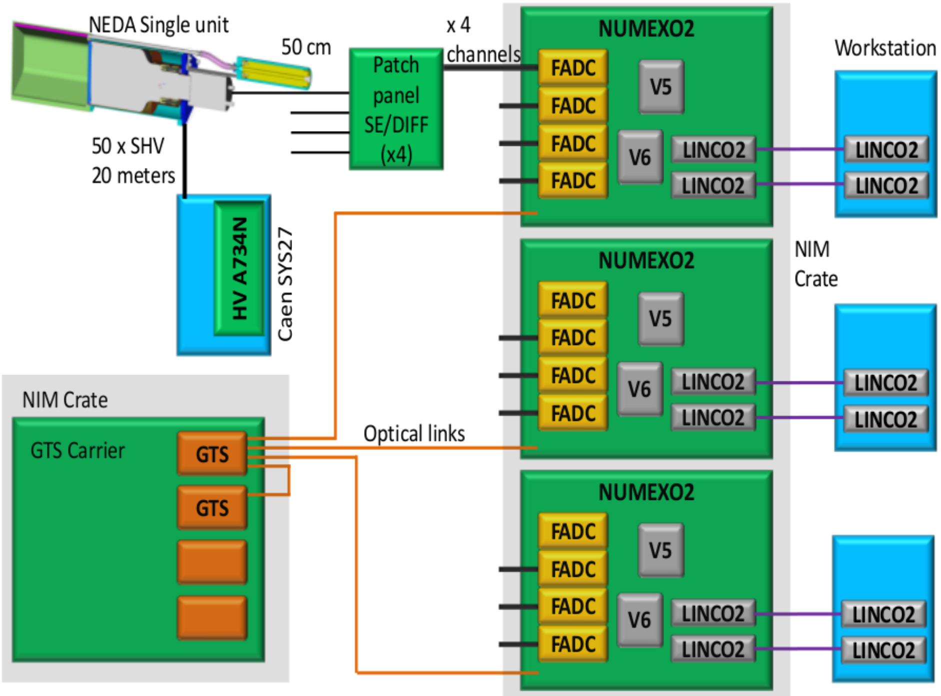

Figure 27: Global electronics layout for the NEDA phase1

Hence, NEDA Phase 0 with 45 detectors requires 3 NUMEXO2 boards, 12 Mezzanines and 6 single-ended to differential boards. However, the final NEDA design, involving totally 355 detection channels require at least of 23 NUMEXO2 boards (placed in 2 NIM crates), 89 FADC Mezzanines, 45 single-ended to differential modules and 3 GTS NIM motherboards containing 12 GTS Mezzanines. Each of the following sections is aimed to describe in details the aforementioned blocks starting from the front-end single-ended to differential board and finishing by the LINCO PCIe boards.

8.2 Description of the Single-Ended to Differential Board

Given that fast pulses, with less than 10 ns rise-time, must be transmitted to the NUMEXO2 digitizer, placed 10m away from the detector in a noisy environment, it was preferred drive through the signals in a differential mode, increasing the immunity against the noise. The first electronic stage the PMT finds at the output is then a small box placed next to the scintillators whose role in the processing is to convert the incoming PMT signals to differential mode before being transmitted over the HDMI cable. Fig. 28 shows the block diagram.

The design contemplates the following functionalities:

- 8-channel single-ended to differential low-noise stages.
- Protection system against high-voltage peaks, avoiding damage on the front-end and back-end electronics.
- A monitor output set before the conversion to differential to display a signal.
- Capability to adjust the gain.

Regarding the design of the single-ended to differential channel, the topology combines both fully-differential amplifiers using the AD8139 for the conversion for the conversion to differential, and

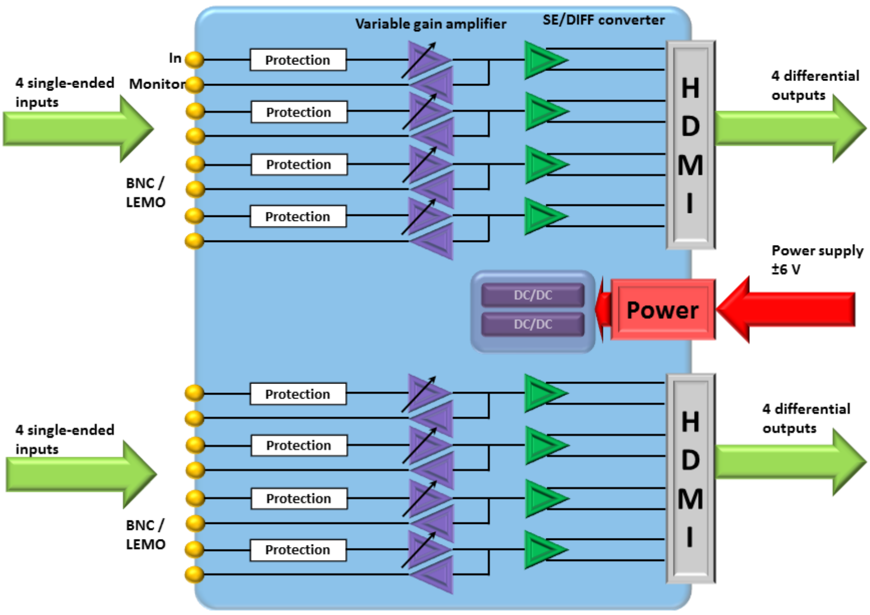

Figure 28: Front-end electronics board.

low-noise operational amplifiers AD4817-1 to provide an easier gain control. To optimize the noise performance on the conversion to differential, a unitary-gain operation mode is selected for the AD8139, while the ADA4817-1 precedes the AD8139 implementing a follower circuit with a potentiometer at the non-inverting input, allowing to control the signal gain. The schematic is presented in Fig. 29.

Figure 29: Front-end electronic channel schematics.

The part preceding the buffer is composed by an overvoltage protection circuit, a smothering capacitor C_s and a terminator in split configuration. The protection circuit is based on low-capacitance (<1.5pF) fast-switching Shottky diodes from the BAV99 series, driving overvoltage peaks towards the power supply, with a current being limited by the 220 resistor. The input terminators R_{T1} and R_{T2} may be configured either for current or voltage inputs. In case of a current input (from a PMT) the current input is transformed into voltage with the input voltage divider point. On the other hand, for standard voltage inputs from a signal generator, is set to R_{T1} $0\,\Omega$ and R_{T2} to its corresponding termination impedance, typically $50\,\Omega$.

8.3 Cable Transmission Features

Due to the fast nature features from the signals, a testbench has been developed to characterize a set of different cables and determining the best solution for NEDA, byapplying bandwidth, crosstalk and EMI tests. The candidates for connection to the front-end are:

- MDSM coaxial cable, containing 19 coaxial connections.
- HDMI cable.
- HDMI v 1.4. Infinite.
- PoCL-Lite camera cable.

The procedure to measure the bandwidth consists of driving sinusoidal input signals with constant amplitude across a frequency sweep, measuring the amplitude degradation at the output versus the frequency. Then, the bandwidth is then calculated as the frequency at which the input amplitude decreases by 3 dB below the input voltage. The results for all cables are shown in Table 6.

Table 6: Cable bandwidths.

Cable under test	−3 dB point (BW)	−6 dB point
MDSM	-	-
HDMI	70 MHz	230 MHz
HDMI v1.4 Infinite	120 MHz	$>$ 240 MHz
PoCL-Lite	35 MHz	130 MHz

Crosstalk tests are performed by driving on one of the pairs a differential pulse and measuring the induced voltage on a second victim pair at the far-end. Specially, it is interesting to study the effect for different edge times, where the measurements have been using for 10ns and 2.5 ns, even though the latter is out of the specifications, aimed mostly to measure the cable robustness against coupling. The waveforms used for this tests consists of driving square waveforms of 1 Vpp. An important remark is to terminate properly tthe unused pairs must be terminated in order to avoid reflections from the victim pairs. Crosstalk measurements are summarized in Table 7 for 10ns and 2.5 ns edge time, obtaining the crosstalk of the differential signal (and not the induced crosstalk on each pair conductor).

Table 7: Crosstalk test comparison table for different cables at different rise / falling times.

Cable	$t_r = 10$ ns	$t_r = 2.5$ ns
MDSM	14 mV	43.8 mV
HDMI	2.73 mV	3.82 mV
HDMI v1.4 Infinite	3.94 mV	8.02 mV
PoCL-Lite	3.16 mV	4.18 mV

Since the experimental area undergoes processes involving radiation, it is of major interest to test the shielding and grounding robustness against high-voltage peaks susceptible to be induced into the cable. EMI measurements can be implemented by applying high-voltage pulses induced to the cable using a conductive surface such as a piece of foil paper embracing part of the cable outer surface. As well as it was performed in the crosstalk measurements, it is required to terminate correctly each unused pair, preventing the cable from undesired reflections which could falsify the measurements. A high-voltage pulse generator NSG1025 from Schaffer was used to inject 1 kV high-voltage pulses of 1 ţs width with a 50 Hz periodicity. Besides, a copper plate was used to ground the whole testbench by grounding the equipment chassis. EMI results for the tested cables are synthetized in Table 8.

Table 8: EMI results for different cables.

Cable under test	Peak-to-peak of the induced voltage for 1 kV voltage peak
HDMI v1.4 Infinite	356 mV
HDMI	1.077 V
PoCL-Lite	6.252 V

In conclusion, according to all the results obtained, the choice for a cable was keen on the HDMI v1.4 Infinte cable since is the only one capable to deal with the NEDA signals by having 120 MHz bandwidth. In addition to the bandwidth results, HDMI v 1.4 infinte shows the best performance in crosstalk, EMI measurements, being finally the most suitable option for NEDA.

8.4 Description of the NUMEXO Front-End Electronics Hardware

NUMEXO2 is the core of the NEDA front-end electronics. The NUMEXO2 digitizer and pre-processing system has been design in synergy with GANIL, providing a common solution for more detection systems, reducing time and resources. Hence, the digitizer functionalities can be summarized in: A/D conversion, data pre-processing, connection to the GTS system and communication links management for 16 channels. The system is composed of a motherboard and the set of 4 FADC Mezzanines in charge to perform the A/D conversion for 4 channels. NUMEXO2 owes its flexibility due to the use of FPGAs (Field Programmable Gate Arrays), facilitating the firmware algorithm design. Particularly, NUMEXO2 comprises 2 high-performance FPGAs (Field-Programmable Gate Arrays), a Virtex-6 and a Virtex-5 from Xilinx. Fig. 30 illustrates the main NUMEXO2 block diagram, including the FPGAs, FADC Mezzanine and communication links.

Figure 30: NUMEXO2 general block diagram.

8.4.1 Power Management

NUMEXO2 is design to be held into the NIM standard crate capable to deliver up to 2000 W from Caen, from which the power supply is delivered to the rest of electronics within the digitizer, including the FADC Mezzanines. For this specific crate the currents provided are: ś6 V (90 A),ś12 (20 A) V ś24 V(10 A), allowing a maximum of 130 W/NUMEXO2 when hosting 12 digitizers in the crate. The usage of FPGAs normally involves a big assortment of different voltages to supply all blocks correctly. Fig. 31 shows the power supply block diagram.

Figure 31: NUMEXO2 power supply distribution.

8.4.2 NUMEXO2 Interface

NUMEXO2 is interfaced outwards by connections both in the front and rear panel. Also, internally is provided of QFS connectors to communicate with the FADC Mezzanines.

- Connections on the front panel
  - The data is driven differentially from the front-end modules using 4 HDMI (19 pins) cables. 12 of those pins are used as inputs while the rest remain grounded. Additionally, a screwing tool strengthens the connection against mechanical vibrations.
  - 2 HDR PoCL-Lite connectors. Used to deliver the power supply to the front-end electronics.
  - 4 double LEMO 00 connectors to drive 4 inspection lines from signals capable to be visualized. Each inspection line can be daisy-chained to another digitizer, requiring 2 connectors per inspection line. From the 4 inspection lines, 2 are digital and 2 are analog.
  - 4 LEMO connectors with the following functionalities: External clock, external acquisition stop, external trigger and output clock.

- Connections on the back panel
  - One RJ-45 connector used for the TCP/IP readout protocol.
  - One RJ-45 connector used to monitor the embedded software booting process using an RS-232 embedded protocol.
  - Two LEMO connectors for hard reset and power off.
  - A SFP optical connector to link the GTS leaf in Virtex-5 to the V3 Mezzanines inside the GTS crate.
  - A SFP optical transceiver for the PCIe data transmission. The connector is provided with 4 bidirectional channels.
  - A SFP connector to provide the clock the the Linco2 boards.
- Internal board-to-board connectors.
  - Each FADC Mezzanine is interfaced to NUMEXO2 using 2 QFS-026-04.25-L-D-PC4 connectors from which the power supply, data, clocks and slow control is provided. 8 connectors are required per digitizer to communicate properly with all the Mezzanines.

8.4.3 Clock Management

The 100 MHz frequency reference of the analog to digital conversion and processing units is delivered by three different sources: The 100MHz clock of the local oscillator, the 100MHz remote clock of an external generator and a 100MHz clock recovered from the GTS system. The choice of the 100MHz source is controlled by software although by default, the 100MHz reference clock is sourced by the local oscillator. The block diagram in Fig. 32 shows two parts:

- The GTS clock part: the 100MHz clock is recovered from the optical communication of the GTS system. Once the GTS is locked by the PLL, the 100 MHz GTS clock is sent to a multiplexer. The delay line aims to tune the fine coarse alignment of the clock phase regarding the timing of the messages recovered from GTS communication.
- The 100 MHz clock selection part: the selected clock is sent to a delay line and to a PLL aiming to tune the phase and to distribute the 100MHz to FPGAs and FADC mezzanines.

Figure 32: NUMEXO2 clock management block diagram.

8.4.4 Readout Requirements

Fig. 33 shows the different requirements in terms of data throughput at several points inside NUMEXO2.

Figure 33: NEDA readout requirements block diagram.

Taking into account that the experimental conditions are expected to work maximally at a counting rate of 50 kHz, the FADC Mezzanine maximum sampling frequency at 250 MHz (in practice it will be used 200 MHz instead), and the 14-bit resolution (in terms of bytes it can be expressed as 2 bytes), the throughputs and data rates can be derived as follows.

Assuming that a data packet to send between both FPGAs is 250 samples, and the counting rate is 50 kHz/channel, it can be calculated the average amount of data per channel 50 kHz * 250 samples

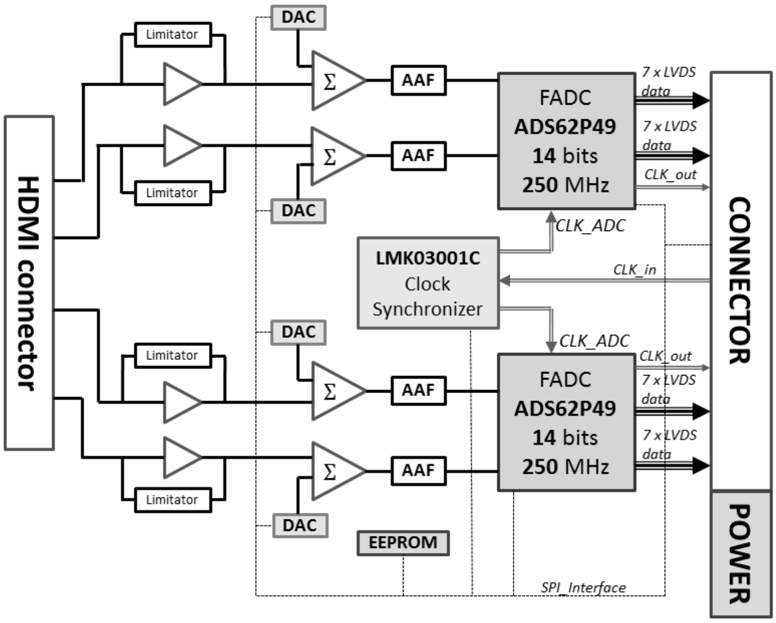

Figure 34: FADC Mezzanine block diagram, including the most important blocks, such as the FADC device, PLL, DACs, operational amplifiers and connectors.

(each containing 2 bytes) leads to 25 MB/s/channel. The fast link between the V6 and V5 contains 8 lanes to drive the data retrieved from 2 channels, rising the total amount of data per lane to 50 MB/s (400 MB/s for all channels). Therefore, taking into account the 4 lanes provided by the PCIe readout in terms of bits/second, it arises to 3.2 Gbps and 800 Mbps per PCIe lane. PCIe maximum data rate is 10 Gbps, verifying the protocol suitability for this application.

8.5 Description of the Sampling FADC Mezzanine

Fig. 34 shows the FADC Mezzanine block diagram. The digitizer chosen for this application is the dual FADC ADS62P49, with 14-bit and 250 Msps. According to the jitter and noise specifications, the rest of devices such as the jitter cleaner, analog coupling stages, DACs, power regulators and connectors have been selected.

The analog input stage coupled with the FADC is the most critical in terms of noise. Additionally, extra offsets are added in order to take full profit of the FADC dynamic range, allowing the acquisition of both unipolar and bipolar signals. After a wide study, the coupling is performed by means of AD8139 fully-differential amplifiers (FDA). At this stage, also the gain control is carried out to select either 6 or 20 MeV. The aforementioned energy ranges can be translated at the level of the Mezzanine as voltage-to-voltage gains, which are, 1 and 0.25 respectively. Due to stability facts, the amplifier must work minimally under unitary gains, as lower gains make it unstable. Moreover, the noise performance conditions are optimal for unitary gain, worsening for higher gains. Due to the noise constraints and stability issues, the design strategy consisted of using two AD8139-based stages working under unitary gain. The attenuation factor of 0.25 can be then achieved by adding a T-divider in between both stages so that the division ratio and the impedance seen backwards from the amplifier can be designed independently. Based on the schema from Fig. 35 the high-speed analog driver can be designed by applying the following expressions:

$$\text{Gain} = \frac{R_{F2}}{R_{G2}} \frac{1}{R_1} \left(\frac{1}{\frac{1}{R_1} + \frac{1}{R_2} + \frac{1}{R_{G2}}} \right) \tag{2}$$

$$R_{F2} = R_{G2} + R_1 || R_2 \tag{3}$$

$$R_T || R_{G1} = 50\,\Omega \tag{4}$$

where R_{Fi}, R_{Gi} refer to the feedback and input resistors of each i-th analog AD8139 stage respectively, R_1 and R_2 are the T-divider resistors, and R_T is the input terminator. Equation 2) must be applied in order to make the AD8139 working as unitary-gain amplifier while 1) is obtained after applying Kirchoffs laws to the T-divider and second stage input nodes. Finally, 3) is used to match the terminator impedance with the cable impedance provided that the cable has 100 Ω differential impedance.

Figure 35: FADC Mezzanine block diagram, including the most important blocks, such as the FADC device, PLL, DACs, operational amplifiers and connectors.

A lower-speed analog driver consists of driving the offset voltages from the DAC towards the high-speed analog stage using a side summing branch. Finally, the analog stage contains an antialiasing filter set before the FADC device. It is based on a single-pole RC filter with 100 MHz cut-off frequency.

Another important point is the connection to the Mezzanine from the front-end electronics. Several quality tests such as bandwidth, crosstalk and EMI were applied to several cables, finally choosing the HDMI 1.4 Infinite as the best solution. The other interface is connected using a two board-to-board connectors to NUMEXO2, connecting slow-control signals, high-speed data, clocks and power nets.

Regarding the power supply design, as the FADC Mezzanine requires several voltages for both analog, mixed and digital devices. The main devices such as the FADC and PLL are supplied by their own LDOs independently. This strategy was not followed only by power consumption and temperature reasons, but also to isolate the noise produced by the clock lines into the A/D converters.

A testbench platform was developed to test the FADC Mezzanine performance, involving on one hand standard A/D conversion parameters such as SINAD, ENOB, THD and, on the other hand parameters linked to the quality of acquisition in the field of nuclear physics, such as the energy resolution and gamma-neutron discrimination performance.

Hence, the Mezzanine is tested using a ML605 Evaluation Module (which contains a Virtex-6 FPGA), to buffer, read out the data and program the FADC Mezzanine via SPI. A second additional board, foreseen as a prototype for NEDA front-end electronics, connects the laboratory equipment to the FADC Mezzanine. The software part is performed using GUI based in LabView to communicate the user with the firmware and the Mezzanine via serial port. Hence, the user is able not only to visualize and handle the Mezzanine registers, but also to watch the data analysis process on-line.

The following describes the parameters that characterize the acquisition system, including measurements of interest for the nuclear physics field. Noise performance from electronics can be calculated only with the baseline using this expression, which is defined in [40]:

$$\sigma_e = \frac{R}{\sqrt{12}} \frac{1}{2^{\text{ENOB}}}. \tag{5}$$

Here σ_e is the noise standard deviation in ADC counts obtained experimentally, and R is the dynamic range, also in ADC counts (16384 counts for 14-bit ADC). The measurements have been applied along the ADC range since the resolution varies depending on the input voltage applied. Fig. 36 summarizes the results obtained for 200 MHz for all channels.

Figure 36: Baseline resolution results in ADC counts. Results have been obtained for all channels at 200 Msps and two bandwidths, 50 MHz (red) and 100 MHz (blue)

The figure reveals that for the baseline levels, which are the extreme and middle values, e is around 1.4 rising up to 2 for some specific cases, verifying the system correct behavior. For e = 1.4, an ENOB of 11.7 is achieved. Energy resolution measurements were performed at GANIL in February of 2014, using ^{60}Co and ^{152}Eu sources. The energy spectra, were measured using the firmware prepared for NUMEXO2 in EXOGAM2 containing a MWD (Moving Window Deconvolution) and the rest of the Data Acqusition system using the Narval core. The results of the spectra are depicted in Fig. 37.

Figure 37: ^{60}Co spectrum and its zoom in the 1.17 MeV and 1.33 MeV peaks.

Based on the spectra calibration using ^{60}Co, the resolution obtained is 2.3 keV at 1.33 MeV.

8.6 Description of the LINCO2 Readout Board

The LINCO2 boards are a set of adapter boards to translate the PCI express signals to/from the optical physical layer to legacy bus standards such as PCI, cPCI, VME, etc. Fig. 38 shows a picture of the LINCO2 board.

Figure 38: LINCO2 board picture.

LINCO2 boards have already been used for AGATA and for CMS at CERN in harsh environmental conditions. Each LINCO2 board contains 4 SFP optical connectors, a set of high-speed multiplexers which allow the selection either of clock or data signals, and, a PLX high-speed switch PEX 8609 capable to work up to 20 Gbps which allows the interface between the optical fibers and the PCIe finger. A Spartan-3A is used to configure the high-speed blocks providing 3 different configurations: capability to transmit 4 clocks, 4 data lanes or 2 clocks and 2 data lanes. In Fig. 39 it is shown the LINCO2 block diagram.

8.7 Description of the Global Trigger and Synchronization System

An upgrade towards a full-digital system requires the implementation a system capable to synchronize all channels and to cope with the event validation/rejection. Inherited from AGATA, and being implemented for the NEDA electronics, this is explicitly the task the GTS carries on. One of the most interesting features it provides is the possibility to use it between different detectors, making possible different combinations of detector coupling.

GTS is based on a tree topology, and it contains three different types of firmware depending on the hierarchical solution: On one side, the aforementioned GTS leafs, at the bottommost position of the tree, which are placed inside the Virtex-5 in NUMEXO2. Out of the digitizer, we find the Fan-in Fan-out and the Root units which are left in an additional NIM crate reserved for the GTS. Both firmware programs (fan-in fan-out and root) can be downloaded into V3 Mezzanines. Each V3 Mezzanine has 1 upstream and 3 downstream optical links, where each upstream link from either the

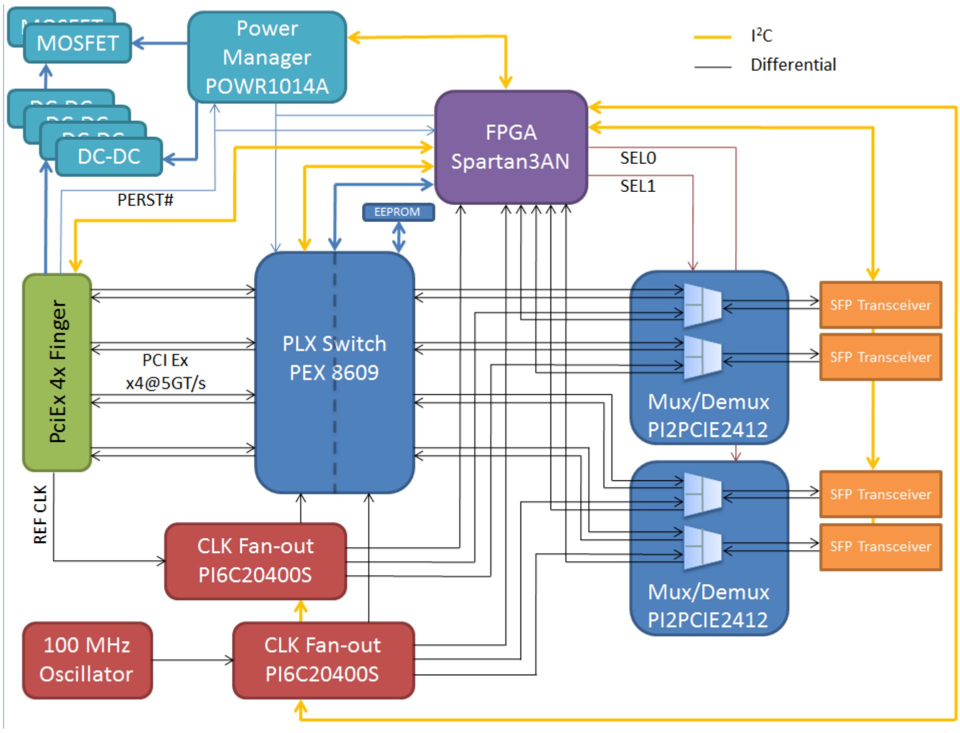

Figure 39: LINCO2 board block diagram.

GTS leaf or a Fan-in Fan-out is connected to a downstream link from the GTS upper level. Finally, all nodes converge at the root node whose upstream link is connected to the trigger processor. The trigger processor is the element in the top of the GTS and it is in charge to cope with the event validation and rejection. Fig. 40 shows the topology of the GTS tree and a picture of the GTS V3 Mezzanines. NEDA, when using 23 NUMEXO2 boards (capable to sample up to 368 channels), requires a total amount of 12 V3 Mezzanine units, 11 of them used as 3-to-1 Fan-in Fan-out units one as a root module, although for the NEDA Phase 1 with 45 channels only requires making use of 2 V3 Mezzanines (1 Fan-in Fan-out and 1 root node) since only 3 NUMEXO2 boards would be used.

Figure 40: Left: GTS tree hierarchical topology. Right: Picture of the GTS V3 Mezzanine, placed in the NIM GTS crate.

8.7.1 GTS Crate interface

The connections of the GTS V3 mezzanine are:

- One SFP connector for the upstream optical link to the top of the tree.
- Three SFP connectors for the downstream optical links to the bottom of the tree.
- Two Mictor connectors for power supply, control and trigger.

GTS V3 mezzanines are provided properly running. Depending on the position of the GTS V3 in the tree, the proper file (root.mcs, fanin-fanout.mcs, leaf.mcs) must be downloaded in its Xilinx PROM. Firmware and embedded software (VxWorks OS) files are fully retrieved from Padova GTS experts working on AGATA project The block diagram of the GTS NIM module depicted in Fig. 41 shows:

- 4 GTS V3 mezzanines implemented in one NIM carrier
- One GTS V3 mezzanine, so called top mezzanine, linked to three GTS V3 mezzanine, so called bottom mezzanines. The three downstream SFP connectors of the top GTS V3 are optically linked to the upstream SFP connector of the 3 bottom GTS V3.
- On the front panel:
  - Nine downstream links of the 3 bottom GTS V3 towards the bottom of the tree. Front panel connectors could be SFPs of the GTS V3 or LC fiber optic adaptors.
  - One upstream link of the top GTS V3 towards the top of the tree. Front panel connector could be SFP of the GTS V3 or LC fiber optic adaptor.
  - One differential PECL 100MHz clock output sourced by one bottom GTS V3 from Mictor connector. Front panel connectors are SMA or double Lemo 00. Jumpers select signals connection to connector pins or to 50 ohm GND pulldown resistor.
  - One differential PECL synchro signal output sourced by one bottom GTS V3 from Mictor connector. Front panel connectors are SMA or double Lemo 00
  - One differential PECL 100MHz clock input, sourcing the top GTS V3, from the Mictor connector. Front panel connectors are SMA or double Lemo 00
  - One differential PECL synchro signal input, sourcing the top GTS V3, from the Mictor connector. Front panel connectors are SMA or double Lemo 00
- On the back panel:
  - One Ethernet 100 link for control purpose of GTS V3. Each mezzanine has an IP number and is addressed through the Mictor connector. An Ethernet switch is implemented to select one over four GTS V3 mezzanines. Back panel connector is RJ45.
  - One serial link for debugging GTS V3. Each mezzanine is addressed though the Mictor connector. Jumpers select one over four GTS V3 mezzanines. Back panel connector is DB9.
  - One NIM connector providing the power for GTS V3mezzanines: +12V, + 3V3 and the GND.
- Inside the module:
  - Four (2*7 pins) JTAG connector devoted to download FPGA firmware files and debugging. Because GTS V3 is provided with its FPGA code programmed into the PROM, downloading action should be avoided. There is one JTAG connector per GTS V3.
  - 50 Ω resistors must be put between each unused PECL 100 MHz clock output pin and GND.

8.7.2 GTS Trigger Processor

Most of the hardware, firmware and software components are retrieved from AGATA. The main hardware component of the trigger processor which is optically connected to the GTS V3 root is a PCIe commercial card plugged in a PC, the Xpress GenV5ă200. A photograph of the trigger processor board is show in Fig. 42.

The trigger processor algorithms to establish either a validation or a rejection can be various depending on the experimental context. The most common algorithm is the multiplicity detection of events within a time coincidence window. When performing this algorithm the trigger processor collects

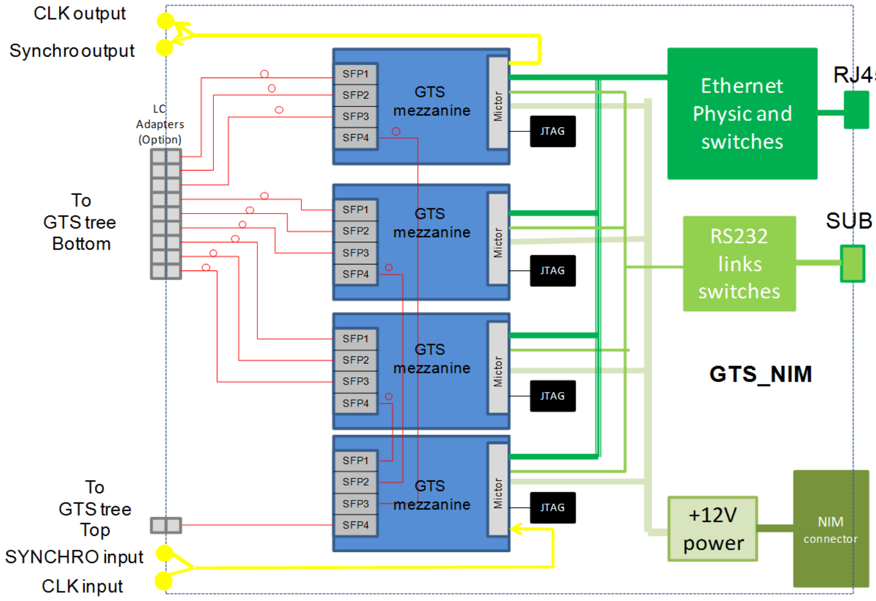

Figure 41: GTS carrier block diagram.

Figure 42: Trigger processor board.

903 the timestamps of the incoming trigger requests. Inside the trigger processor, a time coincidence
904 window used as a buffer is used to compare the timestamps of the surrounding events, providing
905 a validation in case of the number of events within a coincidence overcomes a certain threshold.
906 Fig. 43 shows the algorithm structure.

Figure 43: Multiplicity trigger algorithm implemented in the GTS Trigger processor.

907 8.8 Description of the System Basic Firmware/Software

908 The Virtex-6, concretely the model V6-LX130T is the largest device in NUMEXO2, and carries out
909 most of the pre-processing tasks such as deserialization, triggering algorithms, configuration and
910 oscilloscope. Fig. 44 schematizes all points into a block diagram.

911 8.8.1 Virtex-6 Firmware IPs

912 Input interface ISERDES

913 The first stage of data readout is performed by using a customized arrangement of serialization/de-
914 serialization data sub-blocks (called ISERDES), prepared to work at higher rates than 400 Mbps.
915 Internally, the concatenation of the ISERDES blocks include always their own IODELAY [1], coping
916 properly with the delay adjustment.

917 ISERDES IP has been implemented to deliver at its output four 14-bit outputs, each containing
918 the corresponding even/odd samples of 2 FADC channels as it is shown in Fig. 45, while at the
919 inputs there are 14 LVDS channel, containing even/odd multiplexed bit duplets. The deserialization
920 is performed with a DDR clock latching the odd bits on the rising edge while the even bit do it in

[1]ISERDES and IODELAY sub-blocks belong to Xilinx corporations, as well as the arrangement of those to be prepared to work on for data collection of the ADS62P49.

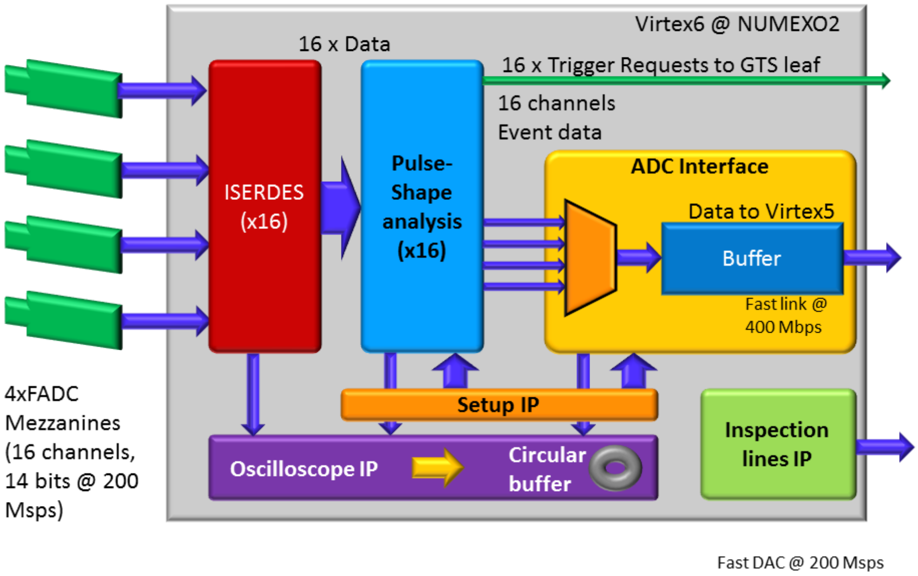

Figure 44: NUMEXO2 Virtex-6 block diagram.

the falling edge, requiring two clock cycles of the FADC output clock to create an output sample at the ISERDES IP output. Additionally, a half-divided clock is delivered too, which is used as the Chip Scope Pro logic analyzer sampling clock.

Figure 45: ISERDES functional block diagram.

Data managment

Sources of NEDA data are the 16 channel samples from FADC mezzanines. Once raw samples are de-serialized, only 250 samples of each channel are kept and sent to the Virtex5. For each of the 16 channels, the selection window is triggered by the digital discrimination of the raw sample input. The protocol is synchronous and 8 bits data are sent on each transition of the clock. The clock transfer and the FADC clock are synchronous.

Oscilloscope IP

Oscilloscope aims to control digital signals at different points of the processing of the 16 channels. Maximum frequency of the 2 byte signal is 200MHz and up to four probes can be simultaneously connected. The binary samples of each probe are continuously stored into a 32kBytes (or 16kWords) circular buffer and its content is frozen as soon as a trigger is occurring. For each probe, the type of trigger and the time can be software-wise controlled:

- Trigger: input threshold, software command.
- Time base: 5ns (FADC sampling frequency), 10ns, 20ns, 40ns, 80ns, 160ns, 320ns, 640ns, 1280ns, 2560ns, 5120ns, 10240ns, 20480ns, 40960ns, 81920ns, 163840ns.

The higher is the time base, the longer is the time inspection window. For example, time base = 163840 ns (1 sample over 32768 samples is kept) gives about 2.68s window

Inspection Lines

Mainly envisaged to monitor internal signals, enhancing the testability of NUMEXO2. At the front panel, 2 analog and 2 digital signals can be visualized using LEMO connectors. The wide assortment of selectable signals can be accessed by means of the internal multiplexers inside the V6 and the 2 fast digital-to-analog (DACs), allowing visualization of analog signals. Among the signals which can be selected, we find the raw-data input, the output of the trapezoidal filter and the analog-wise conversion of the formatted frame which is sent to the V5. Regarding the digital lines, the options lay among the several clock sources, trigger signals from the digital CFD and other internal control lines can be selected.

Set-up register bank

Contains a set of registers used to configure the rest of the blocks within the Virtex-6, aiming to provide a flexible, dynamic and easy-to-configure device. Registers can be read and written using the software tool GECO (Ganil Electronic COntrol), working under the TCP/IP protocol via the Virtex-5. Some of the parameters the setup block takes in charge with are the IODELAY step value, the trapezoidal filter parameters K, M and α, the timescale for the oscilloscope mode and the possibility to either choose parametric or oscilloscope mode in case of using EXOGAM2 electronics via the slow link.

8.8.2 Virtex-5 Firmware IP and Embedded Software

A second programmable device on NUMEXO2 is the device Virtex5FX70T, which manages the data reception from the Virtex-6 after the processing. It manages the communication ports and includes the GTS leaf, linking NUMEXO2 with the GTS. Fig. 46 illustrates the internal blocks multiple blocks inside Virtex-5 which can be described as:

Figure 46: NUMEXO2 Virtex-5 internal block diagram. Courtesy of GANIL.

ADC Interface

The ADC interface block carries out multiple functionalities on the other side of the Virtex-6. Firstly, it receives, unpacks the data frame from Virtex-6 putting it into a buffer and sends the event data to the GTS leaf waiting to be validated / rejected. Also, at this level, if the event was validated from the GTS, the leaf attaches the timestamp received, where the ADC interface takes the data bundled with the timestamp either to the PPC in testing phases of NEDA, or the PCIe through the LINCO2 interface if using NEDA in experiments.

GTS leaf and PLB Cracus IPs

nherited from the AGATA, the GTS system aims to provide synchronization in digital multichannel systems and event accept / rejection. Considering the GTS system a tree-structure, the GTS leaf is hierarchically emplaced at the most bottom part, and it is in charge to receive the events from the ADC interface to the rest of the GTS, placed outside the Virtex-5. Each NUMEXO2 contains one GTS leaf, connected optically to GTS crate and it is capable to manage 16 channels. PLB_cracus is a set of 32 registers of 32 bits which interface the PLB bus and the GTS leaf IP. There are three types of registers: reg_ctrl_i (written by PPC), reg_ctrl_default_i (register values at power on), reg_status_i (read by PPC).

Other functionalities of the leaf is the optical transceiver/receiver control, a clock multiplexer which allows the selection between several input clock sources (local oscillator, recovered from the GTX, and external), providing it to a PLL. Besides, it includes a data path block, aiming to equalize the phase of the GTX and control the data direction (TX or RX), and finally a trigger core, mainly used to exchange messages between the Virtex-6, the trigger request and the transceivers. Finally, at the leaf level, the timestamp is generated and attached to the validated / rejected event. It consists of a 48-bit counter, with a resolution of 10ns. The block diagram of the GTS leaf is depicted in Fig. 47.

The trigger validation / rejection can be sketched easily with the chronogram from Fig. 48. After

Figure 47: GTS leaf block diagram.

the triggering algorithm identifies the pulse likely from a neutron, a trigger request is sent to the GTS leaf. Inside the leaf, it is attached the timestamp, used to tag the moment at which the trigger request was stored with a resolution of 10 ns. Then, the GTS leaf sends the event to the trigger processor, waiting to be validated/rejected. The time lapsed between the trigger request and the notification to the trigger processor is called local latency whose main responsible is the GTS leaf, which is usually 1 clock cycle. Together with the validation/rejection signal is received, the field (named as val_rej_tag[7:0]), contains the timestamp of the event which was previously sent to the trigger processor, where it can be checked the event matching and the number of number of processed event (event count), which is increasing progressively.

Figure 48: GTS chronogram cycle.

Embedded Power PC

Virtex-5 includes a hardware PowerPC (PPC) 440 processor with and embedded Linux OS based, facilitating to cope with the complexity of the TCP/IP protocol. The processor carries in itself a good part of tasks among which we can find the configuration of the rest of blocks inside the Virtex-5, such as the Ethernet Gigabit management, configuration of the PCIe setup registers, the GTS leaf setup (performed through the PLB Cracus IP), interaction with the Virtex-6 setup, FADC Mezzanine SPI registers, B3 registers, as well as the management of external Flash (256 Mb) and DDR (1 Gb) memories and a serial port which allows to monitor the status of the Linux OS booting. Although Virtex-5 can be clock from many sources as we detail in the GTS leaf, the PPC is the only device in the whole NUMEXO2 which must be clocked always from a local clock.

I/O Ethernet/PCIe

NUMEXO2 includes as well an optical link containing 4 PCIe Endpoint lanes, capable to run up to 3.2 Gbps (800 Mbps each), fulfilling NEDA specifications in terms of data throughput. In the middle of the PCIe driver there is a FIFO used to buffer the data between the ADC interface and the driver itself. Fig. 49 shows the block diagram of the PCIe and PCIe_FIFO IPs.

Figure 49: PCIe block diagram.

8.9 Description of the NEDA Trigger Algorithm Implementation

The task of NEDA when being merged with a gamma spectrometer is to provide a clue of the reaction channel for a certain nucleus, using the neutron energy spectra as a depart point. Nevertheless, the neutron detectors based on organic scintillators are sensitive to gamma rays as well, requiring an on-line method to distinguish between the neutrons and gammas. Using a real-time processing technique to deal with the discrimination would increase the overall system efficiency by rejecting the processing of the events produced by the gamma-rays, being only of interest the events produced by neutrons.

Since the study of the particle interaction with matter, a wide set of methods were developed to deal with the discrimination between particles based on the PSA. Although some of the methods provide remarkable discrimination ratios, when dealing with hardware implementation, it was preferred to focus on simple algorithms capable to provide good efficiency. Hence, the goal of the PSA implemented in the FPGA is to provide a first basic discrimination aimed to reduce the events produced by gamma-rays. Two methods are proposed: charge-comparison method and ZCO (Zero Cross-Over) method.

8.9.1 Triggering Algorithms

The charge comparison provides a discrimination clue, based on the integrated charge at different positions of the waveform after the pulse starts. Taking an amplitude-normalized average gamma-ray and neutron waveforms shows that if the waveform is separated between the rising-time and the tail, as the electronics are mostly restrictive in what concerns the fast component, it will not affect to the discrimination. On the other hand, it can be noticed a difference on the pulse tail, due to the behavior of the scintillator. Hence, this method establishes that the ratio δ between the integral on the tail (named as well slow component) and the integral covering the rising edge and part of the damp after the peak (called fast integral), define a parameter to discriminate between neutrons and gammas. An example of gamma and neutron normalized signals is shown in Fig. 50.

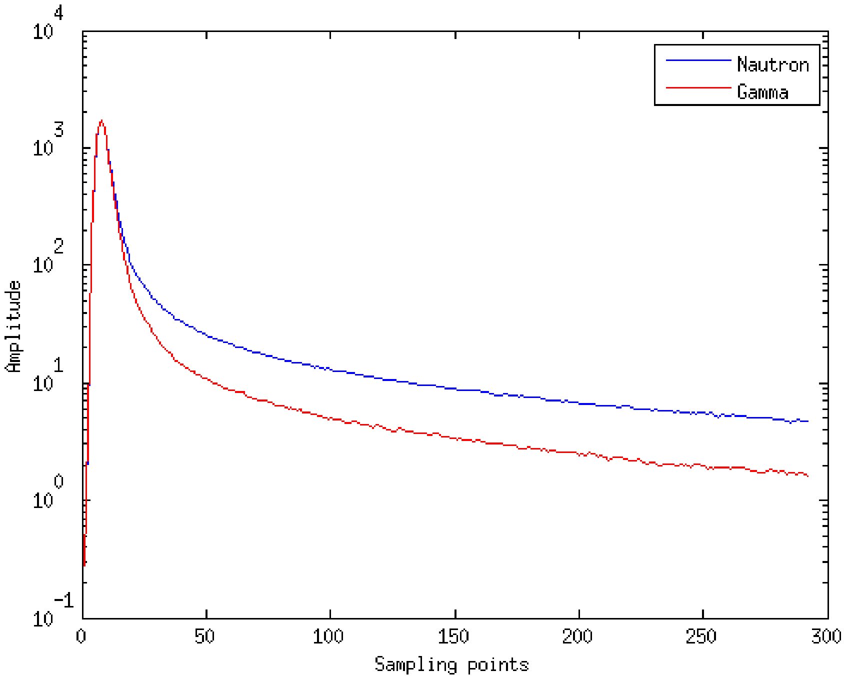

Figure 50: Examples of average neutron (blue) and gamma-ray (red) acquired waveforms. It can be noticed the difference in the decay time, due to way how they deposit their energy in the media.

In the digital domain δ becomes $\widehat{\delta}$, and α and β are defined as the number of samples over which the fast and slow integral components are calculated, hence, integrals become into sums, whose expressions leads to:

$$\delta = \frac{\int_\beta v(t)dt}{\int_\alpha v(t)dt} \rightarrow \frac{\sum_{n=\alpha+1}^{\beta} v(n)}{\sum_{n=1}^{\alpha} v(n)} \tag{6}$$

Even though the charge-comparison method becomes straightforward when implemented digitally, its calibration by analog means entails difficulties due to the usage of two different time gates. Hence, for this reason the method has not been widely used in analog electronics, becoming more popular the zero-crossover method with constant fraction discriminator.

ZCO time in a pulse is defined as the time measured between the pulse beginning and the time at which the signal changes polarity. The ZCO algorithm is based on this approach to lead to particle discrimination by shaping digitally the incoming pulse into a bipolar signal. Hence, the discrimination clue is obtained based on the time between the trigger overcomes the threshold and the zero-crossing point, denoted as ZCO time, as Fig. 51 shows.

In a similar manner analog shapers work, a digital shaper can be designed by means of difference

Figure 51: Description of the zero-crossover method for neutron-gamma discrimination.

equations applying a conversion technique to the original analog transfer function. The resultant signal, hence contains a faster component with positive sign and a slower on the negative part. Comparing the response to the CR-RC, the convolution can be divided in three terms, analogously to the integral and differential terms from the analog response. Additionally a smoothing function is used to average each point to their neighbors. Hence, the function can be separated as:

$$f(t) = h(t) * p(t) = h_s(t) * h_i(t) * h_d(t) * p(t) \tag{7}$$

Where $h_s(t)$ is a smoothing function, $h_i(t)$ the integral term corresponding to the RC part and $h_d(t)$ is the differential term. Finally $p(t)$ makes reference to the input and $f(t)$ is the output. The zero-crossover time is computed between the polarity change and the time when the original signal overcomes the threshold. The quality for the discrimination is dependent also on the time resolution for the ZCO time. Usually it requires interpolation techniques on the polarity change to enhance the resolution.

The comparison has been carried taking both neutron/gamma discrimination performance based on the figure of merit and computational complexity. Based on both algorithms of ZCO based on convolutions and the charge comparison method present a similar figure of merit M. In views of the minor amount resources required, specially in terms of hardware multipliers and control simplicity, finally keening on the charge-comparison method.

8.9.2 Charge-Comparison Method Implementation

he block diagram in Fig. 52 shows how the charge comparison algorithm can be implemented in an FPGA. Given the raw data @ 200 Msps at the input, the algorithm delivers a signal to the GTS if the event detected was likely a neutron.

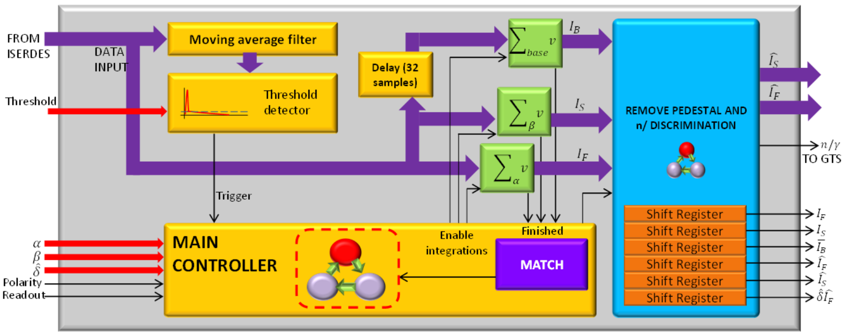

Figure 52: Hardware block diagram of the charge-comparison method.

Taking a closer look to the block diagram, the system architecture consists of a main controller based on a FSM, and a set of slave blocks used for threshold, Integration and pedestal removal. Each sub-block might have as well a local controller inside in case of complex operations. Hence, the blocks are:

- Main controller: Enables/disables the rest of the blocks according to a set of parameters and to a execution sequence.
- Moving average filter: Precedes the threshold detector. By using this filter, the threshold detection avoids spurious noise sources providing more robustness. For this case, an 8-th order moving average is used.

- Threshold detector: Delivers a pulse to the main controller if the signal crosses a certain level set by the user as a parameter.
- Integrators: Using the recursive addition method, the integrators provide the slow, fast and baseline integrals I_{S}, I_{F} and I_{B}, the latter calculated over the 32 samples preceding the trigger. After an integral is finished, it sends a flag to the main controller indicating that the operation has been finished.
- Match unit: A sub-block inside the main controller, takes the flags after integrations are calculated and waits until the last integration is done. Afterwards, it sends a flag to the pedestal correction unit to start the following calculation process.
- Pedestal correction unit and neutron/gamma discrimination: Gathered in the same block due to the reusability of the hardware resources, this multifunctional block calculates both the part of area which shall be subtracted from the pulse and provides the trigger to the GTS after comparing both integrals with the parameter . Besides, it incorporates a set of 6 PISO (Parallel-In Serial-Out) registers in case results of the integration require to be read with a minimal amount of resources from a logic analyzer. Hence, taking as inputs I_{S}, I_{F} and I_{B}, the block delivers:

$$\widehat{I_{\mathrm{S}}} = I_{\mathrm{s}} - \beta \bar{I_{\mathrm{B}}} \tag{8}$$

$$\widehat{I_{\mathrm{F}}} = I_{\mathrm{f}} - \alpha \bar{I_{\mathrm{B}}} \tag{9}$$

$$\begin{aligned} \mathrm{n}/\gamma = 1 \ \text{ if } \ \widehat{I_{\mathrm{S}}} \geq \widehat{\delta}\widehat{I_{\mathrm{F}}} \\ \mathrm{n}/\gamma = 0 \ \text{ if } \ \widehat{I_{\mathrm{S}}} < \widehat{\delta}\widehat{I_{\mathrm{F}}} \end{aligned} \tag{10}$$

To calibrate the values of α, β and $\widehat{\delta}$, a normalized and averaged set of gamma and neutron waveforms have been used. Originally, the samples have been collected by a Strück module @ 500 Msps. Afterwards, the waveforms can be delivered using an arbitrary waveform generator (Agilent 33522A for our case). Analyzing the values of the integrals obtained, Fig. 53 shows the results obtained for several values of α and β.

In Fig.53, it can be seen that for lower values of $\beta < 50$, the discrimination is completely lost. Good discrimination values have been obtained for $\beta = 100$ and $\alpha = 5$ and $\alpha = 6$. After scaling the decimal values of the integrals, and applying a 2^N-power factor to the result of $\widehat{I_{\mathrm{F}}}$, $\widehat{\delta}$ can be chosen as an integer number to facilitate the calculations.

8.10 Cost Table

The NEDA Front-end electronics (FEE), i.e. sampling, pre-processing and readout, has been chosen and developed with the goal of achieving the maximum performance with moderate costs. For the cost table we have taken as reference the FEE required to instrument the NEDA phase 0 version i.e. 45 channels (+ some spare). Fig. 27 shows schematically the electronic parts required. The FEE components list and the corresponding costs are summarized in the Table 9.

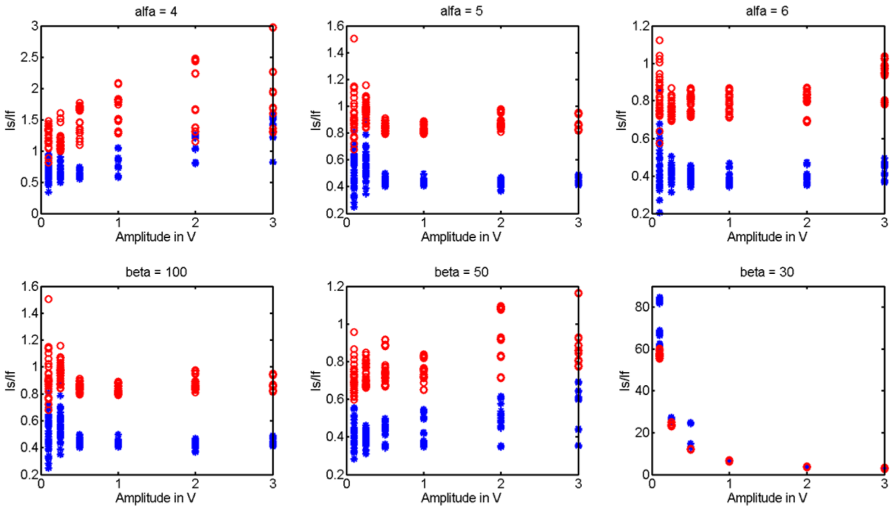

Figure 53: $\widehat{I}_s/\widehat{I}_f$ versus signal amplitude. Upper: sweep across several values setting $\beta = 100$. Lower: sweep across several β values setting $\alpha = 5$. Events produced by γ rays are plotted as stars while neutrons with circles.

Table 9: Estimated costs of NEDA front-end electronics.

Part	Function	Items required	Cost per Item	Total Cost
HDMI adaptor	s-e to diff.	12	(0.25 k€)	(3 k€)
NUMEXO2	Pre-Processing	3	5 k€	15 k€
FADC Mezzanines	Sampling	12	0.67 k€	8 k€
GTS Mezzanines	GTS Tree	2	1.1 k€	2.2 k€
GTS NIM Carrier	GTS Tree	1	1 k€	1 k€
LINCO2	PCI Readout card	6	1 k€	6 k€
NIM Crate	Power supply	1	5 k€	5 k€
Total cost	for 48 channels			40.2 k€

For the complete NEDA the amount roughly scales with the number of detectors.

9 GTS for NEDA

The Global Trigger and Synchronization (GTS) system is responsible for the data synchronization, clock distribution and trigger management in NEDA; as such, it is conceived as a stand-alone system completely decoupled from the readout chain. Its development has been inspired by the TTC (Timing, Trigger and Control) system at CERN LHC [41]. The GTS system is already fully operational in the AGATA experiment since 2009 [42, 43]. Nevertheless it has to be adapted for the NEDA requirements. The main

The NEDA data stream relies on an absolute time being available at the digitization and pre-processing level. This implies the distribution of a high number of phase-locked and phase-matched clocks to all the digitizing modules. The requirements on the GTS system may be summarised as follows:

- the clocks at the sampling FADCs have to be synchronized with a sub-ns precision. This avoids calibration steps that are time-consuming and impractical in NEDA, due to the high number of acquisition channels.
- The system must be able to sustain trigger validations at a rate of 1 MHz with channel multiplicity 1 (e.g. a candidate event made of a single energy deposit in a pre-selected time window), and at a rate of 50 kHz with channel multiplicity 30 (e.g. a candidate event made of up to thirty energy deposits in a pre-selected time window).
- The percentage of trigger loss, namely the trigger requests that can't be processed, has to be lower than a few percents.
- The system has to be scalable: going from 2 to 200 detectors should not induce any conceptual change in the hardware or software involved.

All data sent from one detector are processed on an NIM board called NUMEXO2 carrier that contains in total four mezzanine cards with two FADCs each. A pulse shape analisys algorithm implemented in the core mezzanine issues a trigger request whenever a neutron is discriminated from gamma rays. The GTS system forwards the requests to the global trigger processor and sends back the timestamp identifying the trigger requests. The timestamps of the trigger requests are used by the trigger processor for correlating requests from several detectors in order to possibly validate simple or time delayed coincidences. Upon receiving the trigger timestamp, the readout electronics records a snapshot of the incoming signals, filter them and wait for a possible validation. A validation or rejection of the candidate event eventually arrives from the trigger processor with a maximum latency of 20 microseconds. Several requests can be sent before the arrival of the validation/rejection, hence the validation has to contain the timestamp of the original trigger request. Indeed the order in which trigger requests are sent can differ from the order of validations reception, the sequence depending on the configuration of the trigger rule (e.g. delayed coincidence). Trigger requests and trigger validations include also an identification of the channel that is used by the trigger processor as geographical information for possible partitioning of the complex detector at the trigger level. The acceptance of a timestamp validation to a given channel triggers its local readout.

Table 10: Synchronization types

Sync. type	*Description*
Sampling	Synchronization of the detector signals with the clock phase
Serial Link	Recovery of parallel data words from the serial bit stream
Trigger Requests Alignment	Alignment of trigger data at the input of the pipelined trigger processor
L1 Validations	Synchronization of L1 validation signal with data into the readout pipelines
Event	Assignment of global clock and event number to data fragments in the DAQ path

Readout electronics stores data in internal FIFOs. The system can be immediately rearmed after a trigger request and can accept other trigger requests as long as the internal buffers are not full. The trigger processor, which is the root of the GTS tree, assigns the event number, while forwarding its decision (validation or rejection) to the GTS mezzanine. When the event is accepted, the data are forwarded to the carrier board memory and hence, through a PCI express optical link, to the acquisition computer.

The design of the front-end readout follows a synchronous pipeline model: the detector data are stored in pipeline buffers at the global NEDA frequency, waiting for the global trigger decision. The

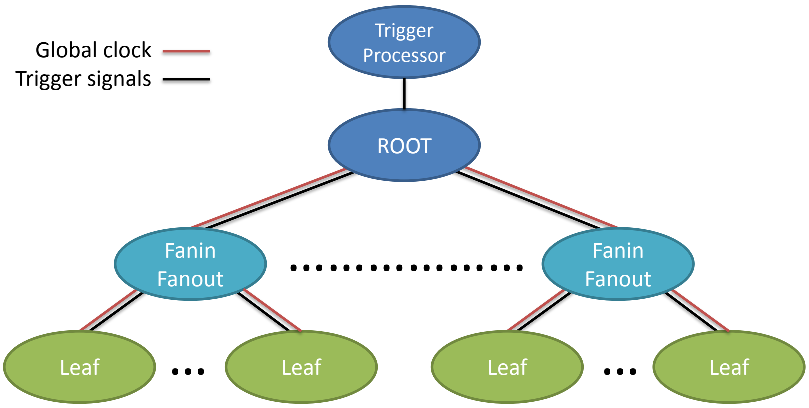

Figure 54: Topology of the GTS system

time between the firing of a trigger request and the consequent validation or rejection is called the trigger latency. This latency is not required to be constant for each trigger request (and actually it is not), but it should fit within the pipeline buffer length. The whole system behaves synchronously; for a proper operation of the system, synchronization at different levels has to be achieved and monitored. Table 10 summarizes the five types of synchronization present in the AGATA readout.

A variable but finite number of global time referenced signals are needed for guaranteeing synchronism of the system elements. In AGATA, they are conveyed through serial optical bidirectional links. These links connect the front-end and readout electronics of each crystal with a central global timing and synchronization control unit in a tree-like structure (Fig. 54). They merge together the three basic functionalities: synchronization distribution, global control and trigger transport.

All GTS nodes provide a fast ethernet connection, which is used for slow control and monitoring. A slow control procedure involving the whole tree allows the synchronization of the clocks. Differntly from the previous versions of GTS, in NEDA one GTS leaf should be able to serve multiple trigger requests in the same timestamp. To this end we need as many trigger request lines as the maximum number of detectors that can ask concurrently for a trigger. The trigger requesters will be implemented in the Virtex6 FPGA of the NUMEXO2 board, while the GTS leaf will be on the Virtex5 FPGA as the buffering of the events waiting for a validation or a rejection. Given the segmentation of the hardware a maximum of 16 trigger requests are expected to be served for each clock cycle.

10 Pulse-Shape Analysis

P.-A. Söderström et al.

11 Time Resolution Measurements with Different Photomultiplier Tubes

11.1 Setup

The time resolution *FWHM* has been measured for the PMT models Photonics XP4512, Hamamatsu R4144 and R11833-100, and ET Enterprises ET9390-kb. The time distribution is obtained from the time difference between coincident γ-rays, using as a reference a fast detector, 3 inch PMT Hamamatsu R2059 coupled to a 1 inch BaF_2 crystal, shielded with μ-metal. Fig. 55 shows a scheme of the setup employed. The detectors were placed at 90° in order to minimize the arrival of scattered

γ-rays from one detector into the other. Additionally, a thick 5 cm led wall is placed in between. This Pb bricks do not make shadows on the detectors from the Co source, while both detectors do not see each other. The HV for all tested PMTs have been set in order to get 1 Volt/MeV, while the reference detector (BaF2) HV is set to -1806 V and place as close as possible. For this detector, the counting rate in singles with the minimum threshold on the CFD (-20 mV) was 40 kHz. It is set to 4 kHz counting rate with a threshold of -40 mV on the CFD. Shape delay is set to 5 ns.

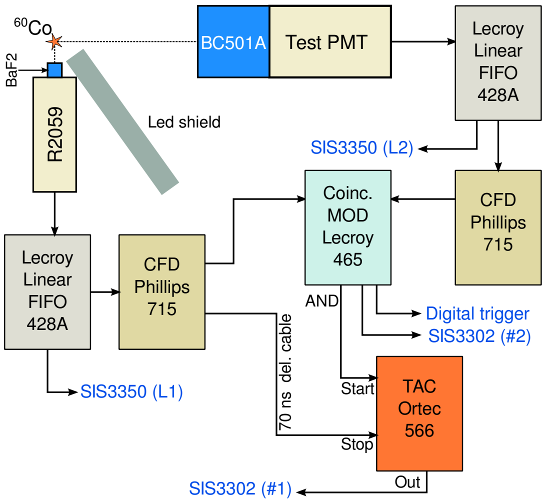

Figure 55: Setup scheme for the detector arrangement and electronics.

In Table 11 is summarized the High-Voltage, threshold (on the scope) and the CFD shaping delay employed in the analog module.

Table 11: Results for all the PMTs measured with R2059/BaF2 as reference.

Detector	HV (V)	Th (-mV)	Δ (ns)
R2059/BaF2	-1806	40(5)	5
XP4512	-1140	35(5)	10
R4144	-1452	40(5)	10
R11833-100	-1390	40(5)	12
ET9390-kb	-1206	30(5)	25

11.1.1 Electronics

The electronic setup is arranged as shown in Fig. 55. Both signals from the detectors are passed through a Lecroy N428A linear Fan-In Fan-Out, from which signals are send to both a ADC for the digital part, and to CFD modules Phillips 715. Analog time difference from both detectors are obtained from an Ortec model 566 TAC (500 ns range), using as start the coincidence signal from both CFDs, from a Lecroy model 465, and a signal from the BaF2 CFD, delayed 70 , as stop. With this setup, both analog and digital time distributions are independently measured. Analog timing was optimized for each detector by using the CFD delays shown in table 11). Digital timing indeed, is obtained regardless the analog electronic chain, as both the waveform from the testing neutron detector and the BaF2 one are sampled using the coincidence signal as a common trigger. The waveforms are digitized with a Flash-ADC from Struck, model SIS3350, with 500 MHz sampling rate and 12 bit, with a 2 Volt dynamic range. Analog TAC and coincidence signal are also digitized through a Struck SIS3302 at 100 MHz sampling rate and 16 bit. The digitizers communicated with the data acquisition system via a VME controller using an optical link. Pulse-timing properties for the testing neutron-detector has been studied at two different sampling rates. For this purposes, the waveforms were downsampled at 200 MHz, using as a filter a discrete averaging with an effective *cutoff* frequency of 100 MHz. The reference detector indeed has been treated always at 500 MHz sampling rate.

11.2 Data analysis and results

Timing resolution of the NEDA array is important for TOF measurements in order to get good n-γ discrimination. In this respect, it is worth to compare how the time resolution obtained by digital means deviates respect to the analog TAC, and study which intrinsic factors, as the rising time and N_{phe} can affect the time resolution obtained from the digitized waveforms, depending on the sampling rate.

Fig. 56 shows the waveforms for the four tested PMTs averaged over 100k signals, from the

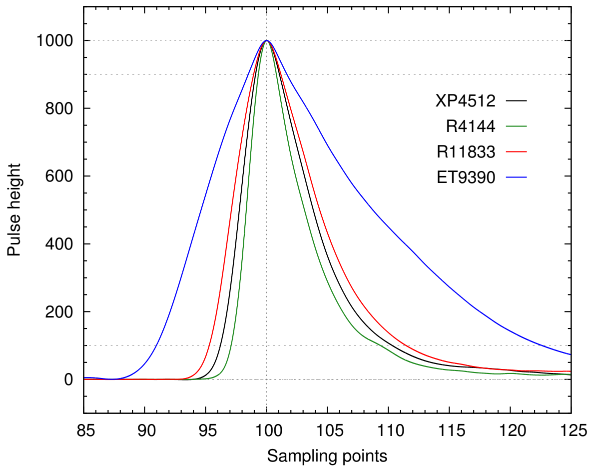

Figure 56: Waveforms averaged over 100k events for the XP4512 (black), R4144 (green), R11833-100 (red) and ET9390-kb (blue) phototubes coupled to 1 inch × 1 inch BC501A cell. All sampled at 500 MS/s. Dashed lines are plot at 10%, 90%, maximum and baseline to guide the eye.

500 MS/s digitizer. An averaged rising time of 3.8(4), 4.9(5), 6.3(8) and 13.5(15) ns is measured for the R4144, XP4512, R11833-100 and ET9390-kb, respectively. The uncertainties here express the *FWHM* for the rising time distribution. The results are shown in Table 12. This indicates that, for the fastest phototubes, a 500 MS/s rate implies only two or three samples on the rising edge, thus, accurate enough timing algorithms should therefore involve necessarily a range of samples larger than the rising edge, specially for less sampling rates.

The algorithm employed for pulse-timing consist on a constant fraction discriminator. Digital constant fraction algorithms has been already studied in different frameworks, such as 100 MS/s sampled waveforms from charge preamplifiers [44], or 2 inch by 1 inch BaF_2 scintillators [45]. This algorithm has been also implemented digitally on FPGA devices employing a linear interpolation of the zero-crossing [46]. Indeed, cubic interpolation for pulse-timing has demonstrate to improve the resolution considerably in certain systems [44].

We develop a CFD from which a cubic interpolation is done to get the zero-crossing. A zero-crossing

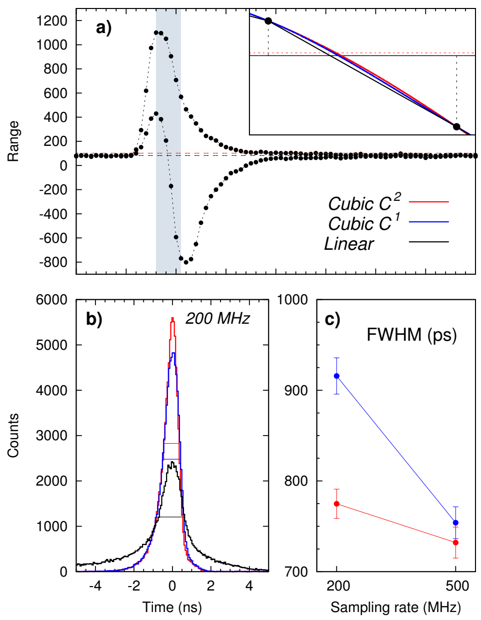

Figure 57: Digital constant fraction algorithm. In *a*) An example of a waveform and the zero-crossing, sampled at 500 MHz. Black dashed line is the *baseline* and red dashed line is the reference to get the zero-crossing. The grey area indicates the samples used for the cubic interpolation C^2. The inset shows the zero-crossing for the three different interpolations. In *b*), the time-difference distribution for the three interpolations are shown, with the test detector downsampled at 200 MHz. *c*) Differences between the cubic interpolation C^1 and C^2 class for 500 and 200 MHz.

signal ZC_i is created by summing the original waveform multiplied by a factor χ and its inverse, delayed an integer number of samples Δ, as indicated in Eq. **??**.

$$ZC_i = \chi \left(S_i - BS\right) - \left(S_{i-\Delta} - BS\right) \tag{11}$$

Here the baseline BS is first calculated and then subtracted from both delayed and scaled components. The zero-crossing point is then obtained by interpolating between the first negative sample and the precedent, at 10 ADC channels over the baseline. The interpolation consists on a cubic spline employing 6 sampling points, with continuous first and second derivatives. Fig. 57 shows the original waveform and the ZC signal for a particular case.

As the zero-crossing reference at constant fraction is thought to remove walking time due to the amplitude in constant rise-time signals [47], the rising time dependence with the amplitude must play a role in the CFD performance. In Fig. 58 we show the risetime for digitized waveforms as a function of the amplitude. There is not apreciable dependence on rise time with the amplitude for any of the detectors. All deviations lie inside the FWHM for the risetime distribution (errorbars in this figure). The largest deviations in risetime at low amplitude respect to the average value occurs for the XP4512 and the R11833-100 models. Such deviations can be presumably responsible of the decrease, at low amplitude, in digital time resolution for such models respect to the analog method, because in the digital algorithm the CFD fraction χ and the delay Δ has been chosen in order to optimize the overall time distribution regardless the amplitude. Time resolution as a function of the energy is shown in Fig. 59 for *a*) the XP4512, *b*) the Hamamatsu models R4144 and *c*) R11833-100 and *d*) the ET9390-kb detector. Number of photoelectrons per MeV were also measured for each detector.

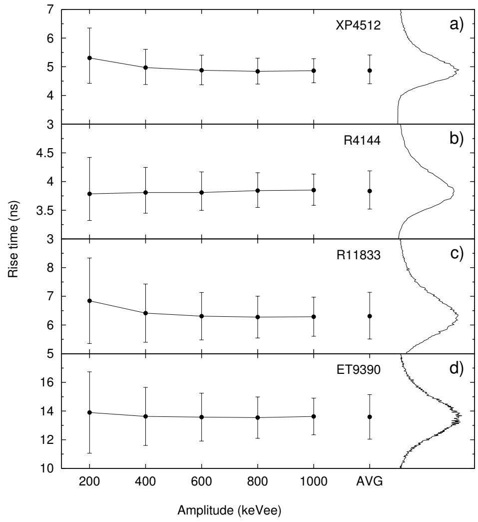

Figure 58: Waveform rising time for different amplitudes for the PMTs *a*) XP4512,*b*) R4144, *c*) R11833-100 and *d*) ET9390-kb mounted with the BC501A cell. The averaged value with threshold at 100 keVee is indicated as AVG and the total distribution is plot on the right. Error bars indicate the FWHM.

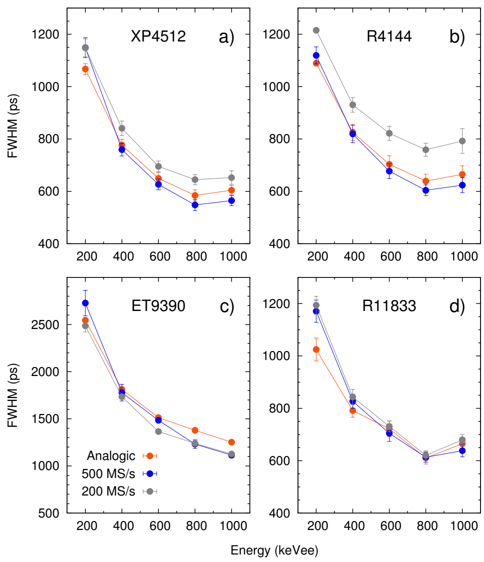

Figure 59: Time resolution FWHM for *a*) XP4512, *b*) R4144, *c*) ET9390-kb and *d*) R11833-100 PMT models as a function of the waveform amplitude.

Table 12: Results for all the PMTs measured with R2059/BaF2 as reference. A *cutoff* of 100 keVee is applied.

			Time resolution FWHM (ps)		
Detector	Risetime (ns)	Nphe (MeV^{-1})	Analogic	500 MS/s	200 MS/s
XP4512	4.9(5)	1330(70)	690(30)	660(30)	740(30)
R4144	3.8(4)	950(60)	750(30)	710(30)	870(30)
R11833-100	6.3(8)	1830(90)	743(13)	730(20)	760(20)
ET9390-kb	13.5(15)	1550(50)	1470(20)	1330(30)	1360(20)

11.3 Discussion

In Table. 12 we show the results for all the detectors. The time resolution is given for the two-detector system, although the time resolution for the Scionix R2059/BaF2 reference detector is much better compared to the 5 inch×5 inch liquid scintillators. One extra measurement has been done using two mounted XP4512 detectors one against the other to estimate the reference-detector intrinsic resolution. A maximum quote for the *FWHM* of 200 ps is reported for that detector.
For all the measures, the digital timing resolution at 500 MHz are better or equal to those found in the analogic way. At high amplitudes, digital 500 MHz performs better than the analog for both XP4512 and the R4144. When downsampling, the worsening in time resolution for each PMT is correlated with the rising time and the number of photoelectrons. Time resolution strongly depends on the number N of photoelectrons emited from the photocathode. This is translated as dependency with the energy as $1/\sqrt{E}$ [48], and also makes the difference between PMTs with different quantum efficiency. The slower, and with higher N_{phe}/MeV PMTs, R11833-100 and ET9390-kb exhibit less degradation in time resolution compared with the 500 MHz case. It is worth to notice the increase in the *FWHM* value at the very end of the energy edge. This could be interpreted as a double-Compton scatter of the γ-ray. The production of light inside the cell over two different spots may decrease the resolution.

12 Neutron-Gamma Discrimination with Different Photomultiplier Tubes

L. Xiaoliang et al.

Should we use "PMT selection" in some section title?

13 New Detector Materials

Q. Nishida et al.

14 Radiation Environment and Safety Issues

Mention the safety issues concerning the liquid scintillator.

15 Production, Quality Assurance and Acceptance Tests

16 Civil Engineering and Installation

17 Installation Procedure

Time sequence of the installation, the necessary logistics from A to Z, including transportation.

18 Time Schedule and Milestones

19 Cost Estimates and Funding

20 Organisation and distribution of responsibilities

21 Glossary

References

[1] J. Dobaczewski et al., Phys. Rev. Lett. 72, 981 (1994).

[2] J. Dobaczewski et al., Phys. Scr. T56, 72 (1995).

[3] T. Otsuka et al., Phys. Rev. Lett. 104, 012501 (2010) .

[4] P. Adrich, Phys. Rev. Lett. 95, 132501 (2005) .

[5] D.D. Warner, J. Res. Natl. Inst. Stand. Technol. 105, 33 (2000) .

[6] D. Vretenar et al., Phys. Rev. Lett. 91, 262501 (2003) .

[7] K. Pham et al., Phys. Rev. C. 51, 526 (1995) .

[8] A. Krasznahorkay et al., Nucl. Phys. A567, 521 (1994) .

[9] S. Akkoyun et al. Nucl. Instr. Meth. **A668** (2012) 26-58.

[10] J. Simpson et al. Acta Phys. Hun., Heavy Ion Physics **11** (2000) 159–188.

[11] C. Ur, LNL Annual Report 2009, p.68.

[12] A. Maj et al., Acta Phys. Pol. **B40** (2009) 565.

[13] J.N. Scheurer, Nucl. Instr. and Meth. **A385** (1997) 501.

[14] G. de Angelis et al., in: Ancillary Detectors and Devices for EUROBALL, editor H. Grawe, GSI Darmstadt, 1998.

[15] M. Palacz et al., Nucl. Instr. Meth. **A550** (2005) 414.

[16] E. Farnea et al. Nucl. Instr. Meth. **A621** (2010) 331.

[17] Geant 4.9.2 Release Notes, `http://geant4.cern.ch/support/ReleaseNotes4.9.2.html`.

[18] M.B. Chadwick et al., Nuclear Data Sheets 107 (2006) 2931-3060.

[19] P.I. Dee and C.W. Gilbert, Proc. of the Royal Society of London. Series A, Mathematical and Physical Sciences **163**, No. 913 (1937), 265.

[20] W.F. Caplehorn and G.P. Rundle, Proc. of the Physical Society. Section A **64** (1951) 546.

[21] G.F. Knoll, *Radiation detection and measurement*, Johh Wiley & Sons, 1989, chapter 15.III.

[22] E. Dekempeneer, H. Liskien, L. Mewissen and F. Poortmans, Nucl. Instr. Meth. **A256** (1987) 489-498.

[23] S. E. Arnell et al. Nucl. Instr. Meth. **A300** (1991) 303.

[24] Saint Gobain Cristals, USA, BC501/BC501A/BC519, data sheet, http://www.detectors.saint-gobain.com.

[25] N.J. Roberts and L.N. Jones, Rad. Prot. Dosim. **126** (2007) 83.

[26] P.Coelho et al. Nucl. Instr. Meth. **A280** (1989) 270–272.

[27] The NDE202 was built by D. Wolski, M. Moszynski, et al. at The Andrzej Soltan Institute for Nuclear Studies, Swierk, Poland.

[28] F.D. Brooks Nucl. Istr. Meth., **4** (1959) 151.

[29] P.-A. Söderström, J. Nyberg, and R. Wolters, Nucl. Instr. Meth. A 594 (2008) 79–89.

[30] M. Moszyński et al., Nucl. Instr. Meth. A 350 (1994) 226–234.

[31] J. Ljungvall, M. Palacz, and J. Nyberg, Nucl. Instr. Meth. A 528 (2004) 741–762.

[32] K. Banerjee et al. Nucl. Instr. Meth. **A608** (2009) 440-446.

[33] G. Jaworski et al., Nucl. Instr. Meth. A 673 (2012) 64–72.

[34] S. Agostinelli et al., Nucl. Instr. Meth. **A506** (2003) 250.

[35] J. Allison et al., IEEE Trans. Nucl. Sci. **53** (2006) 270-278 .

[36] A. Gavron, Phys. Rev. **C21** (1980) 230.

[37] P.R.P. Coelho et al., Nucl. Instr. Meth. **A280** (1989) 270-272.

[38] A. Di Nitto et al., Eur. Phys. J. **A47** (2011) 83.

[39] F. Egea et al., IEEE Trans. Nucl. Sci. **60** (2013) 3526.

[40] L.P.G. Bardelli, Nucl. Instr. Meth. **A560** (2006) 270-272.

[41] B.G. Taylor, IEEE Trans. Nucl.Sci. **45** (1998) 821-828.

[42] M. Bellato, Tech. Rep. hal-00729086, Nov. 2005.

[43] M. Bellato et al., IEEE Trans. Nucl. Sci. **55** (2008) 91-98.

[44] L. Bardelli et al., Nucl. Instr. Meth. A 521 (2004) 480–492.

[45] M. A. Nelson et al., Nucl. Instr. Meth. A 505 (2003) 324–327.

[46] A. Fallu-Labruyere et al., Nucl. Instr. Meth. A 579 (2007) 247–251.

[47] W. R. Leo, Techniques for nuclear and particle physics experiments: a how-to approach, Springer (1994).

[48] B. Bengtson and M. Moszyński, Nucl. Instr. Meth. A 81 (1970) 109–120.